



MASTER SCIENCES DE LA MATIÈRE
École normale supérieure de Lyon
Université Claude Bernard Lyon 1

Report - Spring 2018
Yann-Edwin KETA
M2 Computational Physics

Simple model of active particles

[yketa/active_particles](https://github.com/yketa/active_particles)

[yketa/UBC_2018_Wiki](https://github.com/yketa/UBC_2018_Wiki)

Abstract: We present here the methods and models we have developed or adapted from the study of static or sheared packings of spheres to the study of sheared packings of spheroids. These allow us to investigate the critical behaviours observed at the jamming transition and the other behaviours observed near the rheological transition of packings of soft-core frictionless spheroids. We show that our models give results in good accordance with existing literature and point out interesting phenomena which could give new insights into the jamming transition.

Keywords: *soft matter, computational physics, active matter, non-equilibrium physics.*

Project supervised by:

Joerg ROTTLER
jrottler@physics.ubc.ca
Stewart Blusson Quantum Matter Institute
The University of British Columbia
Vancouver, British Columbia, Canada
<http://www.phas.ubc.ca/~jrottler/>



Contents

Introduction	1
1 Model and method	3
1.1 Model	3
1.1.1 System	3
1.1.2 Interparticle interaction	3
1.1.3 Self-propulsion mechanism	3
1.1.4 Equation of motion and control parameters	5
1.2 Integration method	5
2 Motility-induced phase separation	6
2.1 Spontaneous phase separation	6
2.1.1 Illustration	6
2.1.2 Mechanism	7
2.1.3 Phase diagram	7
2.2 Characterisation	9
2.2.1 Local density probability	9
2.2.2 Fluid to phase separated transition	10
3 Displacement correlation and cooperativity	12
3.1 Displacement correlation	12
3.1.1 Displacement maps	12
3.1.2 Displacement correlation	13
3.2 Cooperativity	16
3.2.1 Cooperativity	16
3.2.2 Varying roational diffusion rate $\tilde{\nu}_r$	16
3.2.3 Varying self-propelling velocity \tilde{v}	18
3.3 Directional displacement correlation	20
3.3.1 Directional displacement correlation	20
3.3.2 Varying rotational diffusion rate $\tilde{\nu}_r$	21
3.3.3 Varying self-propelling velocity \tilde{v}	22
3.4 Overview	23
3.4.1 Varying rotational diffusion rate $\tilde{\nu}_r$	24
3.4.2 Varying self-propelling velocity \tilde{v}	25
4 Shear strain correlation	26
4.1 Plastic deformation	26
4.2 Shear strain	26
4.2.1 Shear strain	26
4.2.2 Shear strain correlation	26
4.3 Real space method	27
4.3.1 Method	27
4.3.2 Results	29
4.4 Collective mean square displacement method	32
4.4.1 Collective mean square displacement	32
4.4.2 Results	34

Conclusion	39
References	40
Appendices	43
A Calculation details	44
A.1 Field auto-correlation	44

Introduction

We can distinguish three general classes of non-equilibrium systems [1]:

- systems relaxing towards equilibrium (*e.g.*, thermal system adapting to its thermostat), even if this relaxation is particularly slow (*e.g.*, glasses),
- systems with boundary conditions imposing steady currents (*e.g.*, sheared liquid, metal rod between two thermostats),
- and *active matter*.

Active matter features systems composed of interacting self-propelled units, *active particles*, each capable of converting stored or ambient free energy into systematic movement [2]. This local energy input, at the origin of self-propulsion, drives the system far from thermodynamic equilibrium [3]. Examples of such materials are ubiquitous in biology and span a great range of length scales, from swarms of bacteria [4] and cell tissues [5], to schools of fish [6] and flocks of birds [7] (see figure 1).



Figure 1: Flocking birds. *source:* Hans Overduin/NIS/Minden/Getty, [8].

Moreover, in many biological phenomena, collective motion of cells is of fundamental importance, such as in the healing of wounds [9] and cancer propagation [10], hence motivating fundamental and theoretical research on the topic, jointly between biologists and physicists [11].

From a physicist's point of view, these systems are particularly interesting because they exhibit surprising phenomena, often defying physical intuition, despite being relatively simple in nature. Such phenomena include swarming, clustering, and non-equilibrium kinetic phase transitions [12, 13]. Their study has motivated the development of artificial active particles for experimental purposes [14, 15], as well as various computational models [3, 11, 12, 16–18].

Our research project, which current development is summarised in the following report, aims at numerically analysing a model system of active matter. This system, inspired by Fily *et al.* [17, 19], consists of Brownian disks with purely repulsive interparticle harmonic potential, each of them performing independent persistent random walks. We will show that despite the simplicity of this model, interesting and surprising phenomena

arise: motility-induced phase separation and long-range correlated displacements and shear strain, even at high times. These phenomena will be characterised and compared with current developments in supercooled liquids and glasses research.

All computer programs with which the presented results were obtained were developed in Python  (and occasionally in bash) and written by the author. All scripts – for simulation and analysis purposes – are available in the GitHub  repository [yketa/active_particles](#). This repository is organised such that it can be used as a Python  package, usable with the provided Conda environment. Simulations and analyses were performed on the Stewart Blusson Quantum Matter Institute cluster.

This report is organised as follows. In [chapter 1](#), we describe our model system, as well as the methods we have used in our simulations. We then review 3 important phenomena observed in our simulations. In [chapter 2](#), we characterise the motility-induced phase separation. In [chapter 3](#), we study the displacement correlations. And in [chapter 4](#), we study the shear strain correlations. In each part, we provide details on the implementation of every calculations.

1 | Model and method

1.1 Model

Our model is inspired by Fily *et al.* [17, 19]. It was chosen both for its simplicity, which should guarantee a quick implementation and an easy replication of results, and for the interesting phenomena it should display according to the aforementioned papers.

1.1.1 System

Our system is two-dimensional and composed of N disks in a square box of length L . To avoid crystallisation, we uniformly distribute particles radii, $(a_i)_{1 \leq i \leq N}$, in the interval $[(1 - I)a; (1 + I)a]$, with a the mean radius and I the polydispersity index, and fix $I = 20\%$. From these, we obtain the system packing fraction $\phi = \sum_{i=1}^N \pi a_i^2 / L^2$.

We impose Brownian dynamics (*i.e.*, we neglect inertia) so that the equation of motion of a single particle is given by

$$\frac{d}{dt} \vec{r}_i(t) = \mu \sum \vec{F}_i(t) \quad (1.1)$$

where $\vec{r}_i(t)$ is the radius vector of particle i as a function of time t , μ is the mobility, and $\sum \vec{F}_i(t)$ is the sum of forces applied on particle i at time t .

1.1.2 Interparticle interaction

Particles interact through a purely repulsive pairwise interparticle harmonic potential, such that the force exerted on particle i by particle j is

$$\vec{F}_{ij}(t) = k(a_i + a_j - ||\vec{r}_i(t) - \vec{r}_j(t)||) \frac{\vec{r}_i(t) - \vec{r}_j(t)}{||\vec{r}_i(t) - \vec{r}_j(t)||} \quad (1.2)$$

where k is equivalent to a spring constant.

This interparticle potential is particularly soft – so soft that it theoretically enables particles to go through each others – and it might seem more appropriate to use harder potentials – with forces which diverge as the distance between particles goes to 0. However, it has been noted by the authors of [17] that such a change affects only qualitatively the collective behaviour of particles. We then keep this potential for its simplicity.

Purely repulsive harmonic potentials, initially proposed by Durian [20] to study foam dynamics, have also been extensively used in numerical studies of the jamming transition of athermal frictionless granular materials [21, 22].

1.1.3 Self-propulsion mechanism

We introduce for each particle i a self-propulsion force

$$\vec{F}_i^{(sp)}(t) = \frac{\vec{v}_i(t)}{\mu} = \frac{v_0}{\mu} \vec{n}_i(t) = \frac{v_0}{\mu} \begin{pmatrix} \cos \theta_i(t) \\ \sin \theta_i(t) \end{pmatrix} \quad (1.3)$$

where v_0 is the single-particle self-propulsion speed.

We then control the angular dynamics of particle i with a Gaussian white rotational noise $\eta_i(t)$ such that

$$\frac{d}{dt} \theta_i(t) = \eta_i(t); \langle \eta_i(t) \eta_j(t') \rangle = 2\nu_r \delta_{ij} \delta(t - t') \quad (1.4)$$

where $\langle \dots \rangle$ denotes an ensemble and time average, and ν_r is the rotational diffusion rate. This model of active Brownian particles [23] describes the behaviour of active colloids used in experiments [14, 15, 24, 25].

What equations 1.3 and 1.4 describe is a persistent random walk. Particles are propelled in a direction which decorrelates smoothly via rotational diffusion with rotational diffusion rate ν_r [1]. Qualitatively, we can give the following representation to ourselves: particles follow straight lines for a time $\tau_r \equiv \nu_r^{-1}$, which is the persistence time, and then change direction at random (see Figure 1.1).

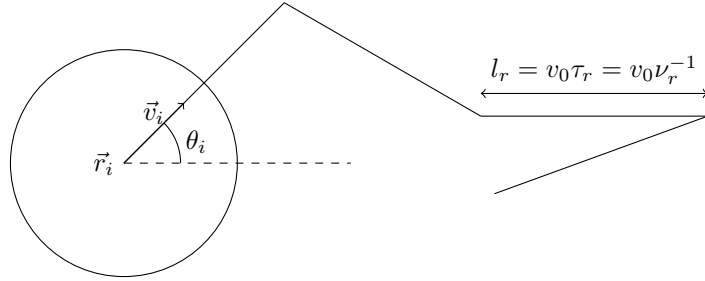


Figure 1.1: Scheme of a persistent random walk. Particle i travels straight lines at velocity v_0 during time $\tau_r \equiv \nu_r^{-1}$, hence travelling the distance $l_r = v_0\tau_r$ which is the persistence length.

It is noteworthy that at low persistence time $\tau_r \rightarrow 0$ (*i.e.*, $\nu_r \rightarrow +\infty$), this self-propulsion mechanism becomes equivalent to thermal agitation [17].

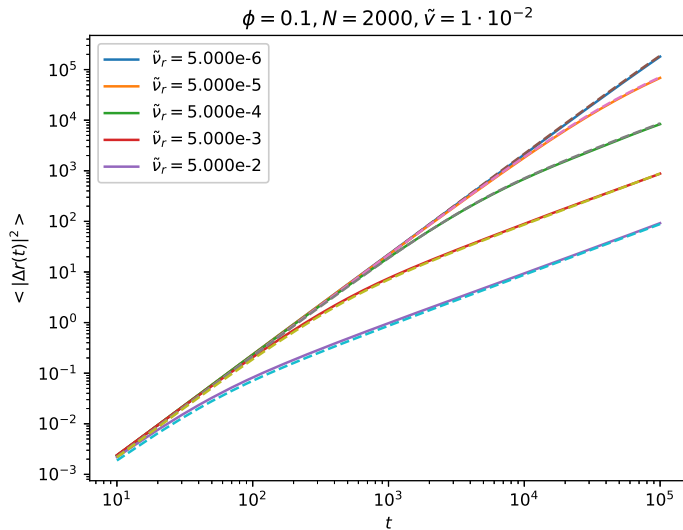


Figure 1.2: Mean square displacement as a function of time $\langle |\Delta \vec{r}(t)|^2 \rangle$ for a system of $N = 2 \cdot 10^3$ particles, with packing fraction $\phi = 0.1$ and dimensionless self-propulsion velocity $\tilde{v} = 1 \cdot 10^{-2}$, for different rotational diffusion rates $\tilde{\nu}_r$. **(solid lines)** Computed mean square displacement at different dimensionless rotational diffusion rates $\tilde{\nu}_r$. **(dashed lines)** Theoretical mean square displacement.

With $\vec{r}(t)$ the radius vector of a single particle as a function of time, we define the mean square displacement as

$$\langle |\Delta \vec{r}(t)|^2 \rangle = \frac{\int dt' ||\vec{r}(t'+t) - \vec{r}(t')||^2}{\int dt'} \quad (1.5)$$

and then introduce the diffusion constant $D_0 = v_0^2/2\nu_r$ such that a single particle performing a persistent random walk described by equations 1.3 and 1.4 has the following mean square displacement at any time t [19]

$$\langle |\Delta \vec{r}(t)|^2 \rangle = 4D_0 \left(t + \frac{1}{\nu_r} (e^{-\nu_r t} - 1) \right) \quad (1.6)$$

in which we observe

$$\begin{aligned} \langle |\Delta \vec{r}(t)|^2 \rangle &\underset{t \rightarrow 0}{\sim} 4D_0 \nu_r t^2 && \Rightarrow \text{ballistic regime} \\ \langle |\Delta \vec{r}(t)|^2 \rangle &\underset{t \rightarrow +\infty}{\sim} 4D_0 t && \Rightarrow \text{diffusive regime} \end{aligned} \quad (1.7)$$

showing that the displacement of the particle is diffusive at high times and with a diffusion constant which increases with increasing persistence time τ_r (*i.e.*, with decreasing rotational diffusion rate ν_r).

This theoretical expression of the mean square displacement gives us a first quick way to test the correct implementation of our model. Indeed, for a low enough packing fraction ϕ , particles should hardly interact with each others. We should thus have that the ensemble mean square displacement

$$\langle |\Delta \vec{r}(t)|^2 \rangle = \frac{\sum_{i=1}^N \int dt' \left| \left(\vec{r}_i(t' + t) - \frac{1}{N} \sum_{j=1}^N \vec{r}_j(t' + t) \right) - \left(\vec{r}_i(t') - \frac{1}{N} \sum_{j=1}^N \vec{r}_j(t') \right) \right|^2}{N \int dt'} \quad (1.8)$$

is given by equation 1.6. We see in figure 1.2 that the theoretical expression in great accordance with the numerical result, hence indicating a correct implementation.

1.1.4 Equation of motion and control parameters

From equations 1.1, 1.2 and 1.3, we can now write the equation of motion of particle i

$$\frac{d}{dt} \vec{r}_i(t) = \mu \left(\vec{F}_i^{(sp)}(t) + \sum_{j \neq i} \vec{F}_{ij}(t) \right) = \underbrace{v_0 \vec{n}_i(t)}_{\text{self-propulsion}} + \underbrace{\mu k(a_i + a_j - \|\vec{r}_i(t) - \vec{r}_j(t)\|) \frac{\vec{r}_i(t) - \vec{r}_j(t)}{\|\vec{r}_i(t) - \vec{r}_j(t)\|}}_{\text{interparticle interaction}} \quad (1.9)$$

which we implement in our simulations.

We finally highlight the 3 control parameters of our model system [17]:

- the packing fraction ϕ ,
- the dimensionless self-propulsion velocity $\tilde{v} = v_0/ak$,
- and the dimensionless rotational diffusion rate $\tilde{\nu}_r = \nu_r/k$ or equivalently the persistence time $\tau_r = \tilde{\nu}_r^{-1}$,

to which we will refer throughout this report.

An additional useful quantity is the dimensionless Péclet number, $\text{Pe} = \tilde{v}/\tilde{\nu}_r = \tilde{v}\tau_r$, which quantifies the dimensionless distance travelled by a single particle before its self-propulsion orientation decorrelates.

1.2 Integration method

Simulations were performed with the HOOMD-blue molecular dynamics simulation toolkit [26–29] on Python . This toolkit was chosen for its high performance on GPUs, its versatility, and its ease of use. Our simulation script is available at https://github.com/yketa/active_particles/blob/main/simulation/collective_migration_DPD_polydisperse_active.py.

Initialisation

After setting the mean radius of particles $a = 1$, we choose the number n_s of different radii to be taken uniformly in the interval $[0.8; 1.2]$. As the algorithm runs slower with increasing n_s , we set $n_s = 10$ and then attribute to each particle one of these different radii. We choose the packing fraction ϕ and then set the length L of the square box accordingly.

We start by positioning particles randomly in the system box. We then use the Fast Inertial Relaxation Engine (FIRE) algorithm [30] to decrease particles' interpenetrations.

Integration

We set periodic boundary conditions and make use of the Brownian integrator as well as the active force functionality of HOOMD-blue for integration of equation 1.9.

2 | Motility-induced phase separation

2.1 Spontaneous phase separation

2.1.1 Illustration

$N = 2.00e + 03, \phi = 0.50, \tilde{v} = 1.00e - 02, \tilde{v}_r = 5.00e - 06, L = 1.128e + 02$
 $t = 0.00000e + 00, \Delta t = 5.00000e + 02$

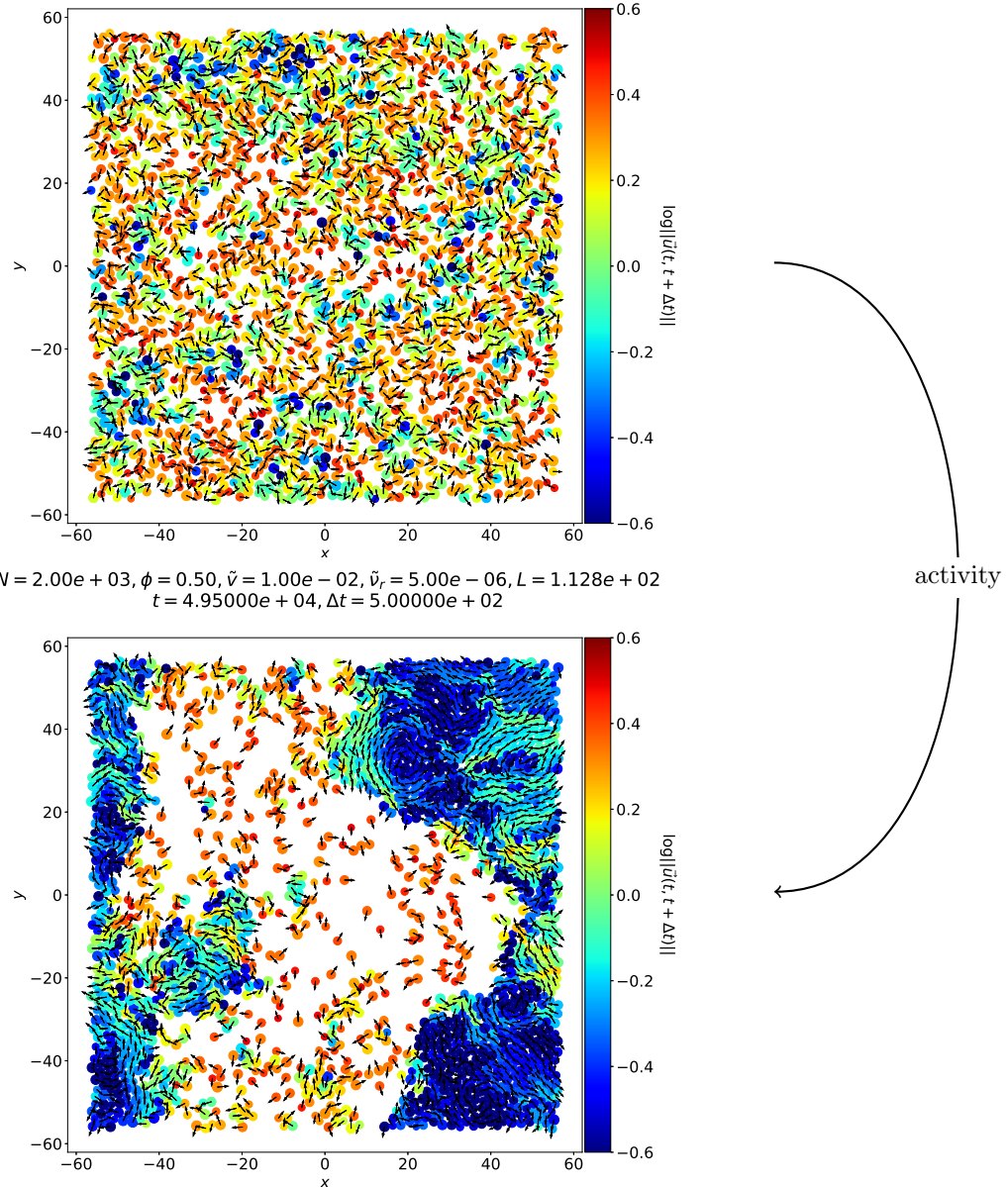


Figure 2.1: Displacement maps obtained with our model system. We denote $\vec{u}(t, t + \Delta t)$ the displacement vector of a particle between times t and $t + \Delta t$. Arrows are aligned with the displacement vector of the corresponding particle (disk). Colors correspond to the amplitude of the displacement vector if the corresponding particle (disk) as reported on the color map. **(top)** Initial state of the system, after applying the FIRE algorithm. **(bottom)** Final state of the system, after integration of the equation of motion (equation 1.9). Movie on GitHub [GitHub](#).

Spontaneous phase separation is undoubtedly the most visual phenomenon we can observe with our model system. As illustrated by figure 2.1, an initially homogeneous system is able to spontaneously separate into two distinct phases:

- an active gas phase, where particles are seldom in contact and thus can move fast,
- and a dense fluid phase, where the motility of particles is greatly reduced.

It is a common feature of systems of self-propelled particles and has been thoroughly explored [3, 16–19, 31].

This phenomenon is particularly counter-intuitive if one thinks about the behaviour of passive colloids at equilibrium. Despite the lack of an attractive interparticle potential, particles seem to be inevitably attracted by each others and form clusters. We describe in part 2.1.2 the underlying mechanism.

2.1.2 Mechanism

Within a system of motile particles, a phase separated state can arise if the speed of particles decreases sufficiently steeply with increasing local density. A dilute active gas then coexists with a dense liquid of substantially reduced motility. This phenomenon is called *motility-induced phase separation* [1].

Its mechanism, described extensively in [1], relies on two ingredients:

- (i) Particles tend to accumulate where they move more slowly, this being inferred directly from the master equation of a self-propelled particle of spatially varying speed.
- (ii) Particles tend to move more slowly where they accumulate. In our case, we see that coarse-graining interparticle forces in equation 1.9 will result in an effective and lesser self-propulsion force.

We then have a positive feedback loop between (i) a slowing-induced accumulation and (ii) an accumulation-induced slowing, which destabilises the uniform suspension. This destabilisation eventually leads to the phase separation we observed.

2.1.3 Phase diagram

We do not observe motility-induced phase separation for every set of parameters $(\phi, \tilde{v}, \tilde{\nu}_r)$. In order to build a phase diagram, *i.e.* to identify which sets of parameters lead to phase separation, Fily *et al.* propose two characterisations of the system.

Mean square displacement

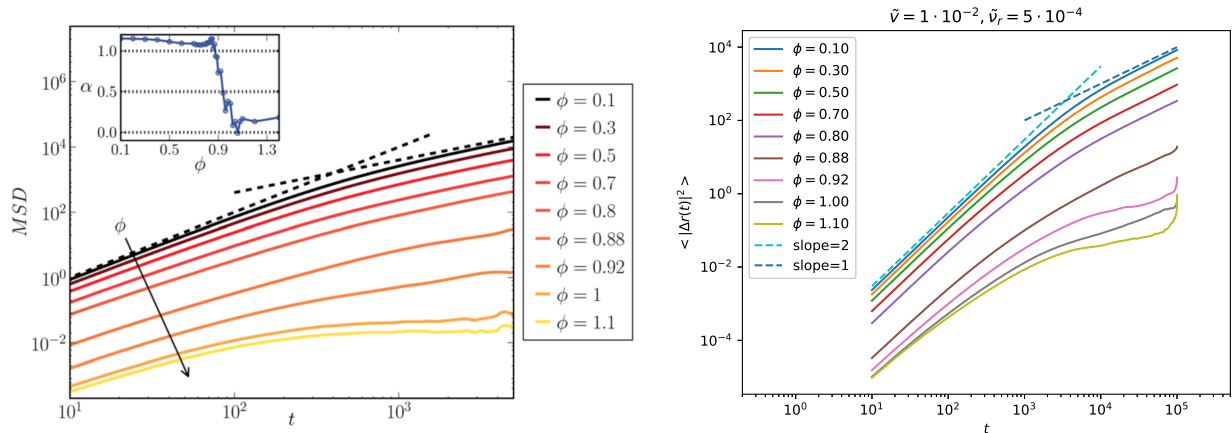


Figure 2.2: Mean square displacement as a function of time $\langle |\Delta \vec{r}(t)|^2 \rangle$ for a system of $N = 2 \cdot 10^3$ particles, with dimensionless self-propulsion velocity $\tilde{v} = 1 \cdot 10^{-2}$ and dimensionless rotational diffusion rate $\tilde{\nu}_r = 5 \cdot 10^{-4}$, for different packing fractions ϕ . **(left)** Data from Fily *et al.*. Inset: Exponent α as a function of the packing fraction ϕ . *source:* [17] **(right)** Data from our simulations. The upward trend at high times observed for the highest packing fractions ϕ is due to the lack of statistics.

We know from the study of glass-forming materials [32] that, at very low temperatures, particles may get temporarily trapped in cages formed by their neighbours – they are in a "frozen" state, in opposition to a liquid

state where they can move more freely. This is shown in mean square displacement (equation 1.8) plots where, at low temperature, $\langle |\Delta \vec{r}(t)|^2 \rangle$ reaches a plateau which height is related to the size of the cage and which length is related to the amount of time the particle stays trapped.

We have observed in our model system that, for a given set of parameters $(\tilde{v}, \tilde{\nu}_r)$, the mean square displacement can be linear (diffusive regime) at low packing fraction ϕ (see equation 1.7 and figure 1.2) and reach a plateau (caged regime) at high packing fraction (see figure 2.2).

Thus, in order to systematically identify "frozen" and liquid states, the authors of [17] introduce the exponent α characterising the long-time time-dependence of the mean square displacement

$$\langle |\Delta \vec{r}(t)|^2 \rangle \underset{t \rightarrow +\infty}{\sim} t^\alpha \quad (2.1)$$

and arbitrarily choose a threshold value, $\alpha_x = 0.5$, separating "frozen" states ($\alpha < \alpha_x$) and liquid state ($\alpha > \alpha_x$) (see inset of left figure 2.2).

Number fluctuation

To identify phase separated regions, the authors of [17] measure the spatial variance $\langle [\Delta N]^2 \rangle$ of the number of particles in a subsystem as a function of the average number N_s in these subsystems. For large enough subsystems, $N_s \gg 1$, this function is a powerlaw of exponent β

$$\langle [\Delta N]^2 \rangle \underset{N_s \rightarrow +\infty}{\sim} N_s^\beta \quad (2.2)$$

With $\tilde{T} = k_B T / (ka^2)$ the dimensionless temperature in a thermal system, they also introduce the thermal counterpart of exponent β in the limit of zero temperature, $\beta_0 = \lim_{\tilde{T} \rightarrow 0} \beta$.

With

$$\beta_e = \beta - (\beta_0 - 1) \quad (2.3)$$

the authors then define phase separated states as states for which $\beta_e > \beta_x = 1.5$.

We propose an other characterisation of phase separated regions in section 2.2.

Phase diagram

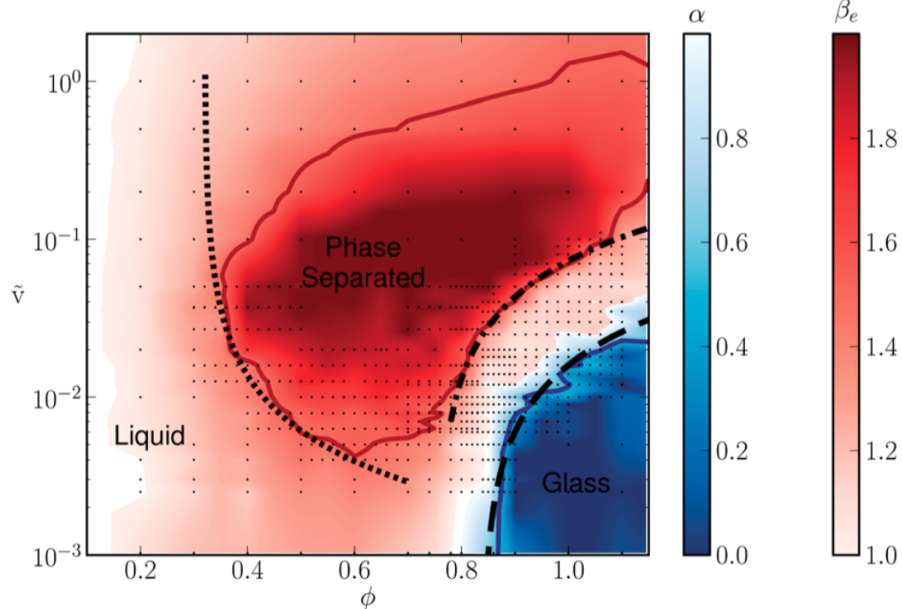


Figure 2.3: Phase diagram of the system, with fixed rotational diffusion rate $\tilde{\nu}_r = 5 \cdot 10^{-4}$, as a colormap of the exponents α (see equation 2.1) and β_e (see equations 2.2 and 2.3). Phase separated states ($\beta_e > \beta_x = 1.5$) are represented in red and glass ("frozen") states ($\alpha < \alpha_x = 0.5$) are represented in blue. The remaining phase diagram space corresponds to liquid states. source: [17]

Exponents α and β_e have been systematically measured for different sets of parameters $(\phi, \tilde{v}, \tilde{\nu}_r)$ by the authors of [17] in order to access the phase diagram of the system (see figure 2.3).

We observe that phase separated states only exist in a range of self-propelling velocities \tilde{v} . For $\tilde{v} \ll 1$, we expect that the effect of activity might be negligible so that the system resembles a packing of athermal frictionless disks, which cannot phase separate and which jams at high packing fraction ϕ [21, 22]. For $\tilde{v} \gg 1$, we expect the interparticle interactions to be negligible in comparison to the self-propulsion term in equation 1.9, thus preventing the accumulation-induced slowing leading to phase separation.

The authors also looked at the evolution of the boundaries between the phase separated states and the liquid states and between the liquid states and the "frozen" states while varying the rotational diffusion rate (see figure 2.4).

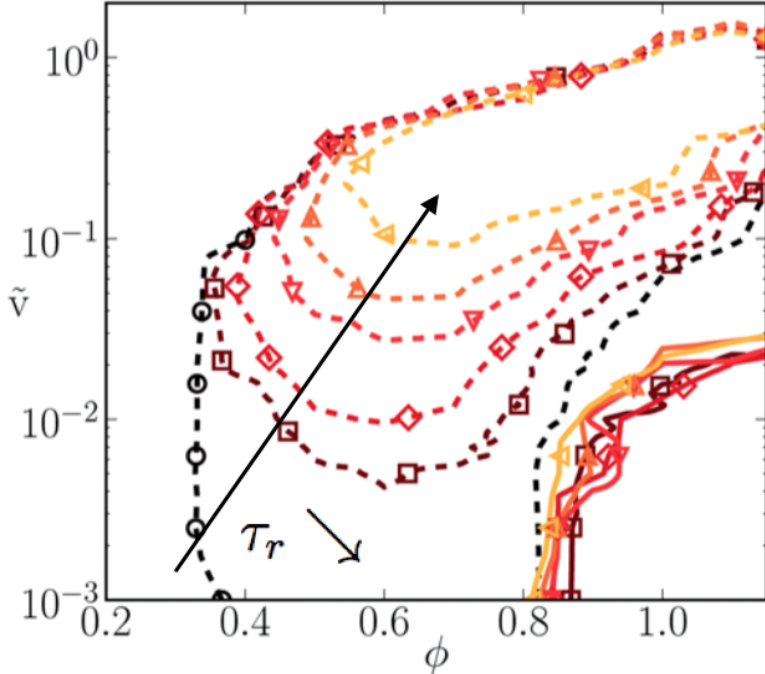


Figure 2.4: Boundaries of phase separated states (dashed lines) and "frozen" states (solid lines) for different dimensionless rotational diffusion rates, $0 \leq \tilde{\nu}_r \leq 1 \cdot 10^{-2}$. We remind that the persistence time is $\tau_r = \tilde{\nu}_r^{-1}$. source: [17]

We observe that the domain of "frozen" states is almost not affected by the rotational diffusion rate, while the domain of phase separated states increases in volume with increasing persistence time τ_r (*i.e.*, decreasing rotational diffusion rate $\tilde{\nu}_r$).

2.2 Characterisation

2.2.1 Local density probability

Rather than characterising phase separated states with number fluctuations, we will more simply measure the distribution $P(\phi_{loc})$ of local packing fractions ϕ_{loc} , as Wysocki *et al.* [16]. This distribution must be unimodal for fluid states and centred around the system packing fraction ϕ , while it must be bimodal for phase separated states with two local maxima at the average packing fractions of the dense fluid phase and the active gas phase.

We define the local density at position \vec{r} and time t as

$$\phi_{loc}(\vec{r}, t, r_{max}) = \frac{\pi}{4r_{max}^2} \sum_{i, ||\vec{r}_i(t) - \vec{r}||_\infty \leq r_{max}} a_i^2 \quad (2.4)$$

where r_{max} is chosen to be a few particle diameters.

Computation details

We divide the system square box in $N_{cases} \times N_{cases}$ linearly spaced square boxes with centres $(\vec{R}_{kl})_{1 \leq k, l \leq N_{cases}}$. We then choose S_{max} times $(t_m)_{1 \leq m \leq S_{max}}$, with $\forall m, t_m \geq S_{init}$ and compute the local densities $(\phi_{loc}(\vec{R}_{kl}, t_m, r_{max}))_{1 \leq k, l \leq N_{cases}}$ then the histogram of the values $P(\phi_{loc})$.

Our computation script is available at [Q yketa/active_particles/analysis/varn.py](#).

2.2.2 Fluid to phase separated transition

We can plot local packing fraction histograms as functions of any parameter of the set $(\phi, \tilde{v}, \tilde{\nu}_r)$, with the two other parameters being fixed, to identify the values of these parameters at the transition between the fluid and phase separated states.

Varying self-propulsion velocity \tilde{v}

As expected from the phase diagram (figure 2.3), we have from figure 2.5 that

- at low Péclet number Pe (*i.e.*, low self-propelling velocity \tilde{v}), the distribution $P(\phi_{loc})$ is unimodal and centred around the system packing fraction ϕ , thus indicating a fluid state ;
- at high Péclet number Pe (*i.e.*, high self-propulsion velocity \tilde{v}), the distribution $P(\phi_{loc})$ is bimodal, thus indicating a separation between regions of high packing fraction (a dense fluid) and vanishing packing fraction (an active gas).

This plot shows that the transition from the fluid state to the phase separated state, when varying \tilde{v} and keeping $(\phi, \tilde{\nu}_r)$ constant, might be continuous. Nonetheless, we do not rule out that additional simulations at self-propelling velocities close to the transition would show a sharper change in the distribution $P(\phi_{loc})$.

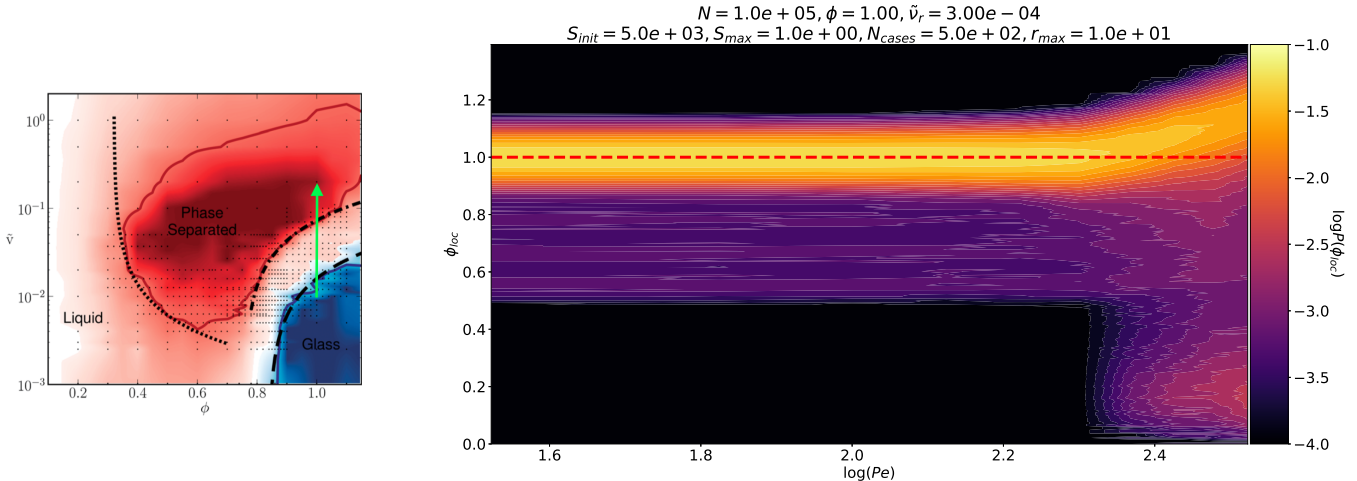


Figure 2.5: (left) (figure 2.3) Phase diagram of the system, with fixed rotational diffusion rate $\tilde{\nu}_r = 5 \cdot 10^{-4}$. Phase separated states are colored in red and "frozen" states are colored in blue. The green arrow represents the path in phase diagram corresponding to the local packing fraction histogram plot. *source: [17]*. (right) Local packing fraction histogram as function of the Péclet number $Pe = \tilde{v}/\tilde{\nu}_r$. Colors correspond to the probability $P(\phi_{loc})$ of the local packing packing fraction ϕ_{loc} as reported on the color map. The red dashed line corresponds to the system packing fraction $\phi = 1.00$.

Varying rotational diffusion rate $\tilde{\nu}_r$

As expected from the phase diagram (figure 2.4), we have from figure 2.6 that

- at low Péclet number Pe (*i.e.*, high rotational diffusion rate $\tilde{\nu}_r$ and low persistence time τ_r), the distribution $P(\phi_{loc})$ is unimodal and centred around the system packing fraction ϕ , thus indicating a fluid state ;

- at high Péclet number Pe (*i.e.*, low rotational diffusion rate $\tilde{\nu}_r$ and high persistence time τ_r), the distribution $P(\phi_{loc})$ is bimodal, thus indicating a separation between regions of high packing fraction (a dense fluid) and vanishing packing fraction (an active gas).

This plot shows that the transition from the fluid state to the phase separated state, when varying $\tilde{\nu}_r$ and keeping $(\phi, \tilde{\nu})$ constant, might be continuous. Nonetheless, we do not rule out that additional simulations at rotational diffusion rates close to the transition would show a sharper change in the distribution $P(\phi_{loc})$.

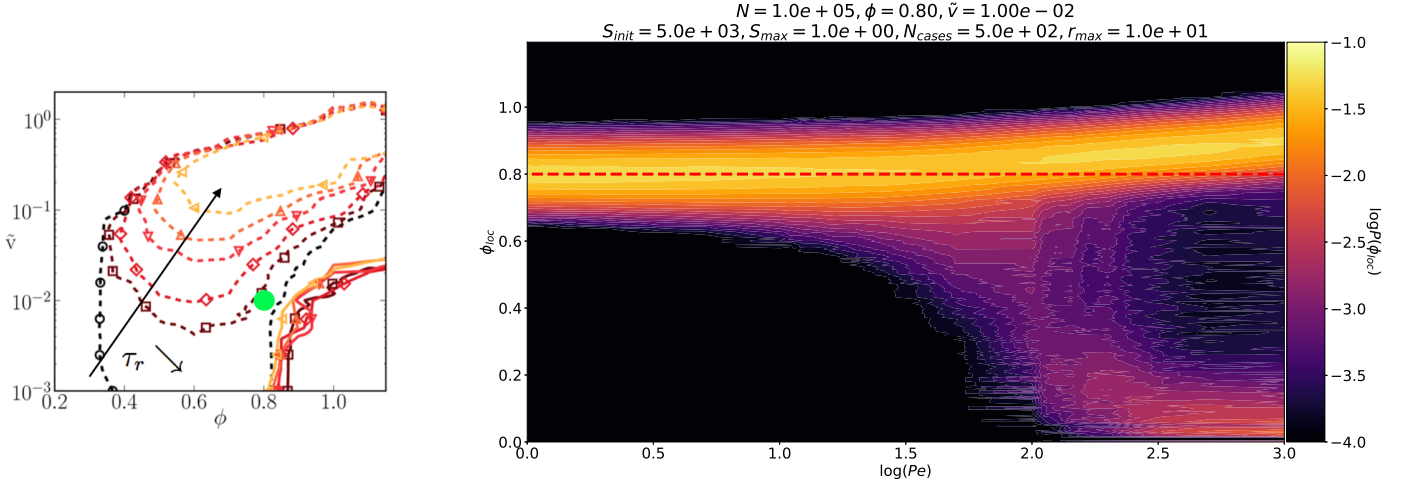


Figure 2.6: (left) (figure 2.4) Boundaries of phase separated states (dashed lines) and "frozen" states (solid lines) for different dimensionless rotational diffusion rates. The green dot marks the set of parameter $(\phi = 0.80, \tilde{\nu} = 1 \cdot 10^{-2})$ corresponding to the local packing fraction histogram plot. *source:* [17]. (right) Local packing fraction histogram as function of the Péclet number $\text{Pe} = \tilde{\nu}/\tilde{\nu}_r$. Colors correspond to the probability $P(\phi_{loc})$ of the local packing packing fraction ϕ_{loc} as reported on the color map. The red dashed line corresponds the system packing fraction $\phi = 0.80$.

3 | Displacement correlation and cooperativity

3.1 Displacement correlation

3.1.1 Displacement maps

$N = 1.00e + 05, \phi = 0.80, \tilde{v} = 1.00e - 02, \tilde{\nu}_r = 1.00e - 02, L = 6.308e + 02, L_{new} = 1.000e + 02$
 $t = 5.00000e + 04, \Delta t = 1.00000e + 02$

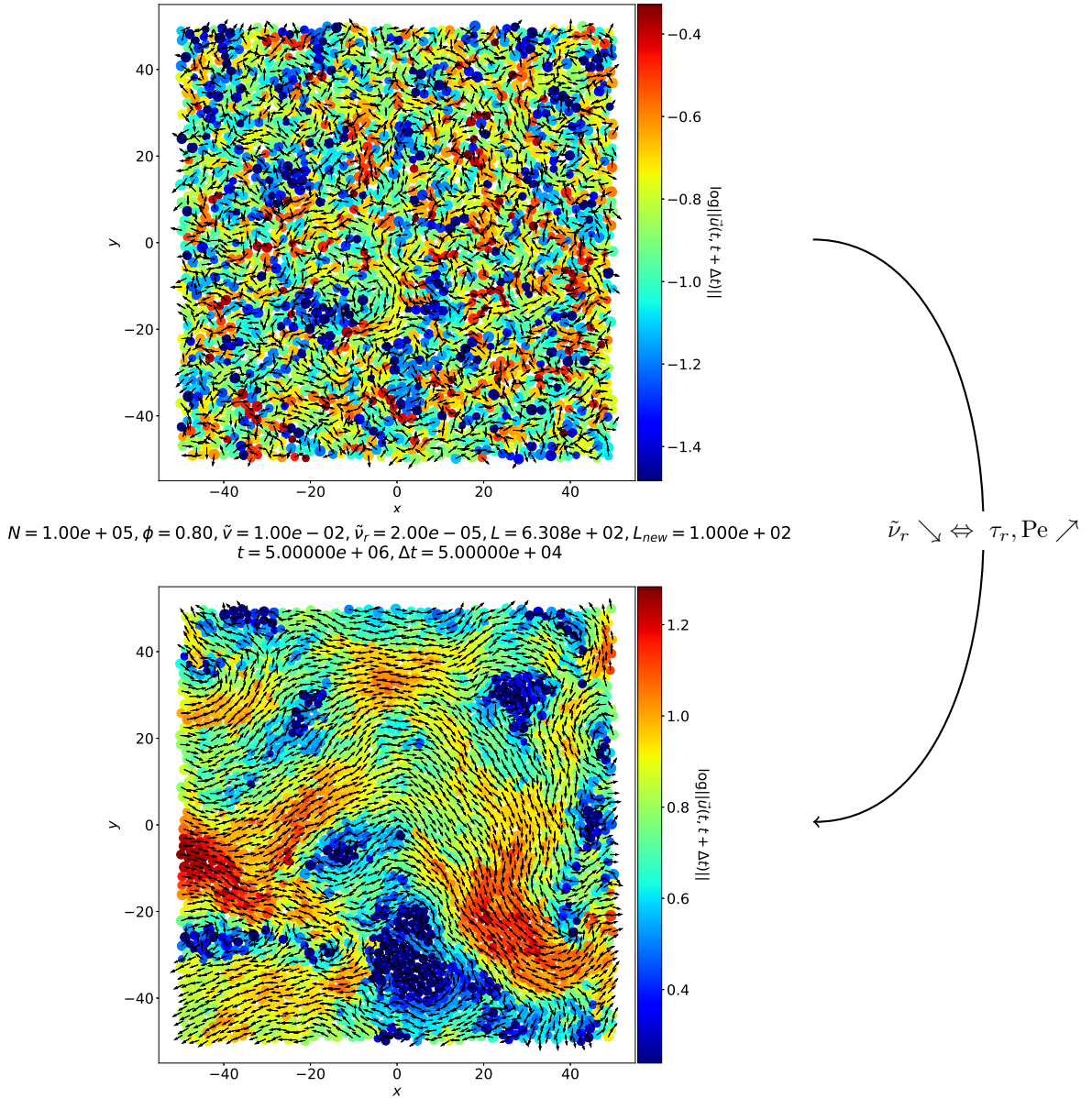


Figure 3.1: Displacement maps obtained with our model system, at packing fraction $\phi = 0.80$ and dimensionless self-propelling velocity $\tilde{v} = 1 \cdot 10^{-2}$. We denote $\vec{u}(t, t + \Delta t)$ the displacement vector of a particle between times t and $t + \Delta t$. Arrows are aligned with the displacement vector of the corresponding particle (disk). Colors correspond to the amplitude of the displacement vector if the corresponding particle (disk) as reported on the color map. We chose Δt such that $\tilde{\nu}_r \Delta t = 1$. **(top)** Low activity system, $\tilde{\nu}_r = 1 \cdot 10^{-2}$. [Movie on GitHub](#) **(bottom)** High activity system, $\tilde{\nu}_r = 2 \cdot 10^{-5}$. [Movie on GitHub](#) .

We observe in figure 3.1 that:

- At low activity (low persistence time τ_r and Péclet number Pe, and high rotational diffusion rate $\tilde{\nu}_r$), displacements vary greatly between neighbouring particles, both in amplitude and direction.
- At high activity (high persistence time τ_r and Péclet number Pe, and low rotational diffusion rate $\tilde{\nu}_r$), neighbouring particles form blocks of similar displacements, both in amplitude and direction. Moreover, the global displacement of neighbouring blocks vary greatly in space and in time (watch [movie on GitHub](#)): this is an evidence of dynamic heterogeneity [33].

To characterise how similar the displacements of neighbouring particles are, we compute displacement correlations in our systems in section 3.1.2.

3.1.2 Displacement correlation

Definition

We define $\vec{u}(\vec{r}, t, t + \Delta t)$ as the displacement vector of the particle at position \vec{r} at time t between times t and $t + \Delta t$. We thus define the displacement correlation of particles separated by $\Delta\vec{r}$ during a lag time Δt as

$$\begin{aligned} C_{uu}(\Delta\vec{r}, \Delta t) &= \langle \vec{u}(\vec{r} + \Delta\vec{r}, t, t + \Delta t) \cdot \vec{u}(\vec{r}, t, t + \Delta t) \rangle_{\vec{r}, t} \\ &= \frac{\int dt \int d^2\vec{r} \vec{u}(\vec{r}, t, t + \Delta t) \cdot \vec{u}(\vec{r} + \Delta\vec{r}, t, t + \Delta t)}{\int dt \int d^2\vec{r} \|\vec{u}(\vec{r}, t, t + \Delta t)\|^2} \\ &= \frac{\mathcal{F}^{-1}\{\int dt \|\mathcal{F}\{\vec{u}\}(\vec{k}, t, t + \Delta t)\|^2\}(\Delta\vec{r}, \Delta t)}{\int dt \int d^2\vec{r} \|\vec{u}(\vec{r}, t, t + \Delta t)\|^2} \end{aligned} \quad (3.1)$$

and assume isotropy in our system such that only the radial part of this correlation function, $C_{uu}(\Delta r, \Delta t)$, will be considered. We refer to appendix A.1 for calculation details leading to the last line of equation 3.1.

We stress that it is usual not to look at the correlation between the simple displacements of the particles but rather between the deviation of these displacements from the mean displacement of the system, *i.e.* the mobility $\delta\vec{u}(\vec{r}i, t, t + \Delta t) = \vec{u}(\vec{r}, t, t + \Delta t) - \langle \vec{u}_i(\vec{r}, t, t + \Delta t) \rangle_{\vec{r}}$. We note however that within our system, which is not externally driven, we have verified that $\delta\vec{u}(\vec{r}, t, t + \Delta t) \sim \vec{u}(\vec{r}, t, t + \Delta t)$. We will thus continue with the simple displacement correlation.

Properties of this correlation function are:

- (i) $\forall(\Delta r, \Delta t)$, $-1 \leq C_{uu}(\Delta r, \Delta t) \leq 1$
 - $C_{uu}(\Delta r, \Delta t) = 1$ (respectively -1) means the displacements of particles distant of Δr during a lag time Δt are perfectly correlated (respectively anti-correlated).
 - $C_{uu}(\Delta r, \Delta t) = 0$ means the displacements of particles distant of Δr during a lag time Δt are completely independent.
- (ii) $\forall \Delta t$, $C_{uu}(\Delta r = 0, \Delta t) = 1$ since the displacement of a given particle is perfectly correlated with itself.

Moreover, particles which are infinitely distant must have completely independent displacements, therefore $\lim_{\Delta r \rightarrow +\infty} C_{uu}(\Delta r, \Delta t) = 0$.

To characterise how similar the displacements of neighbouring particles are, we will look at the spatial extent of $C_{uu}(\Delta r, \Delta t)$ which should indicate a typical distance over which the displacement of particles are correlated.

Please note that it would also be possible to define $\vec{u}(\vec{r}, t, t + \Delta t)$ as the displacement vector of the particle at position \vec{r} at time $t + \Delta t$ between times t and $t + \Delta t$. It has however been observed that both definitions give similar results regarding $C_{uu}(\Delta r, \Delta t)$. Furthermore, we consider that the definition given here is more consistent with the physical signification of $C_{uu}(\Delta r, \Delta t)$ we are interested in.

Computation details

We work with systems with up to $N = 1 \cdot 10^5$ particles, it is then not computationally efficient to evaluate pairwise correlations between displacements of each particles, as done in [34]. We have in equation 3.1 that $C_{uu}(\Delta\vec{r}, \Delta t)$ can be computed from the Fourier transform of $\vec{u}(\vec{r}, t, t + \Delta t)$. We will then rather take advantage

of the powerful Fast Fourier Transform algorithm to speed up our calculations. Nonetheless, to be able to use this algorithm, we have to put the displacement field on a grid, such as we describe thereafter.

We divide the system square box in $N_{cases} \times N_{cases}$ linearly spaced square boxes with centres $(\vec{R}_{kl})_{1 \leq k, l \leq N_{cases}}$. With dL the length of each box, we introduce

$$\vec{u}_{kl}(t, t + \Delta t) = \text{mean} \left(\left\{ \vec{u}(\vec{r}_i(t), t, t + \Delta t), \|\vec{r}_i(t) - \vec{R}_{kl}\|_{+\infty} \leq \frac{dL}{2} \right\} \right) \quad (3.2)$$

the average displacement of particles in each box between times t and $t + \Delta t$. We then choose S_{max} times $(t_m)_{1 \leq m \leq S_{max}}$, with $\forall m, t_m \geq S_{init}$.

We now have $\forall m$, a displacement grid $(\vec{u}_{kl}(t_m, t_m + \Delta t))_{1 \leq k, l \leq N_{cases}}$ of which we can take the Fast Fourier Transform

$$(\tilde{\vec{u}}_{kl}(t_m, t_m + \Delta t))_{1 \leq k, l \leq N_{cases}} = \mathcal{F} \{ (\vec{u}_{pq}(t_m, t_m + \Delta t))_{1 \leq p, q \leq N_{cases}} \} (\vec{K}_{kl}, t_m, t_m + \Delta t) \quad (3.3)$$

with $(\vec{K}_{kl})_{1 \leq k, l \leq N_{cases}}$ the grid of wave vectors, then compute the displacement correlation grid

$$C_{uu}(\vec{R}_{kl}, \Delta t) = \frac{\mathcal{F}^{-1} \left\{ \left(\sum_m \|\tilde{\vec{u}}_{pq}(t_m, t_m + \Delta t)\|^2 \right)_{1 \leq p, q \leq N_{cases}} \right\} (\vec{R}_{kl})}{\sum_m \sum_{p, q} \|\vec{u}_{pq}(t_m, t_m + \Delta t)\|^2} \quad (3.4)$$

and finally use the isotropy hypothesis to calculate

$$C_{uu}(r \in \mathcal{R}, \Delta t) = \left\langle C_{uu}(\vec{R}_{kl}, \Delta t) \right\rangle_{\vec{R}_{kl}, \|\vec{R}_{kl}\|=r} \quad (3.5)$$

where $\mathcal{R} = \{\|\vec{R}_{kl}\|, \forall k, l \in [\![1; N_{cases}]\!]\}$.

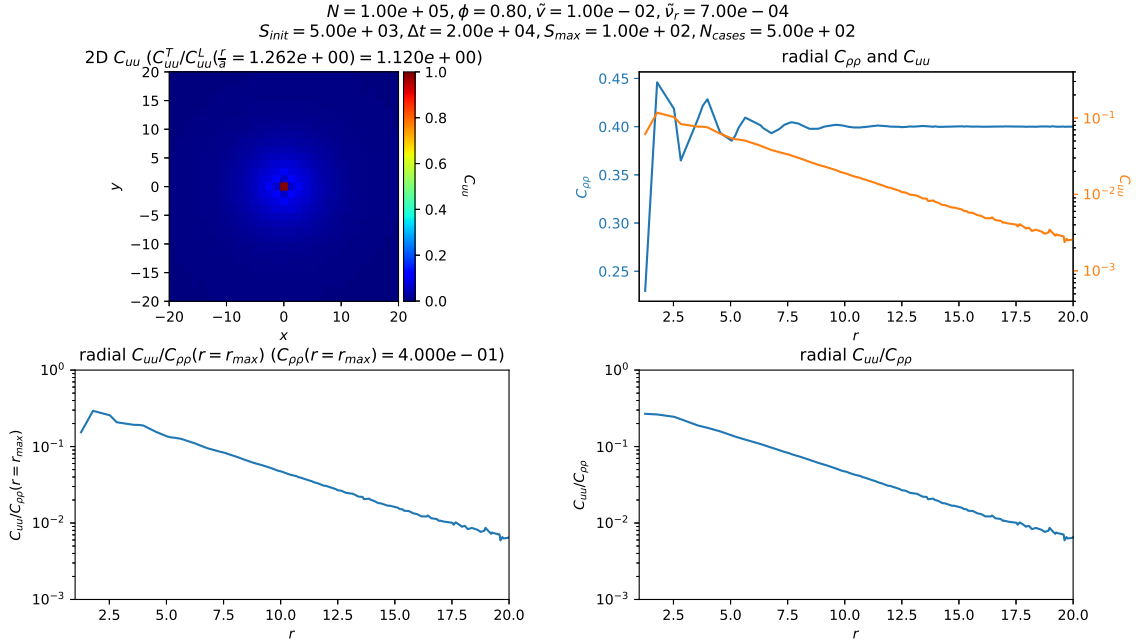


Figure 3.2: Comparison plots of displacement correlation $C_{uu}(r, \Delta t)$, density correlation $C_{\rho\rho}(r)$, and their ratio. **(top left)** 2D map of displacement correlation $C_{uu}(\vec{r} \equiv (x, y), \Delta t)$. We note the circular symmetry of this 2D map, which motivates our isotropy hypothesis. **(top right)** Displacement correlation $C_{uu}(r, \Delta t)$ and density correlation $C_{\rho\rho}(r)$. **(bottom left)** Displacement correlation $C_{uu}(r, \Delta t)$ divided by the plateau value of the density correlation, $C_{\rho\rho}(r = r_{max}) = 4 \cdot 10^{-1}$. **(bottom right)** Ratio of the displacement and density correlation.

We note that while increasing N_{cases} increases the number of radii at which $C_{uu}(r \in \mathcal{R}, \Delta t)$ is calculated, it can also increase the number of boxes with no particles, hence with $\vec{u} = \vec{0}$ according to equation 3.2. At low radii

$r \in \mathcal{R}$, $C_{uu}(r, \Delta t)$ will then be affected by the discrete nature of the system. Consequences of this are lower values of the computed correlation and unphysical oscillations, as illustrated by figure 3.2.

To take this effect into account, we introduce $\forall m$, the density grid $(\rho_{kl}(t_m))_{1 \leq k, l \leq N_{cases}}$ associated to the displacement grid $(\vec{u}_{kl}(t_m, t_m + \Delta t))_{1 \leq k, l \leq N_{cases}}$ such that

$$\forall k, l, \rho_{kl}(t_m) = \begin{cases} 1 & \text{if } \vec{u}_{kl}(t_m, t_m + \Delta t) \neq \vec{0} \\ 0 & \text{if } \vec{u}_{kl}(t_m, t_m + \Delta t) = \vec{0} \end{cases} \quad (3.6)$$

and compute the density correlation grid

$$C_{\rho\rho}(\vec{R}_{kl}) = \frac{\mathcal{F}^{-1} \left\{ (\sum_m |\tilde{\rho}_{pq}(t_m)|^2)_{1 \leq p, q \leq N_{cases}} \right\} (\vec{R}_{kl})}{\sum_m \sum_{p,q} |\rho_{pq}(t_m)|^2} \quad (3.7)$$

then its one-dimensional counterpart in the isotropy hypothesis

$$C_{\rho\rho}(r \in \mathcal{R}) = \left\langle C_{\rho\rho}(\vec{R}_{kl}) \right\rangle_{\vec{R}_{kl}, ||\vec{R}_{kl}||=r} \quad (3.8)$$

which function is

- constant and equal to 1 for low enough N_{cases} ,
- and proportional to the pair-distribution function [35] for high enough N_{cases} .

We have verified that $C_{uu}(r, \Delta t)/C_{\rho\rho}(t)$ gave consistent results with any value of N_{cases} , thus indicating that this is the correct displacement correlation function within our computation method. Without further notice, we will then always consider this ratio rather than the bare displacement correlation function.

Our computation script is available at [Q yketa/active_particles/analysis/cuu.py](#).

Displacement correlation comparison for a set of (ϕ, \tilde{v})

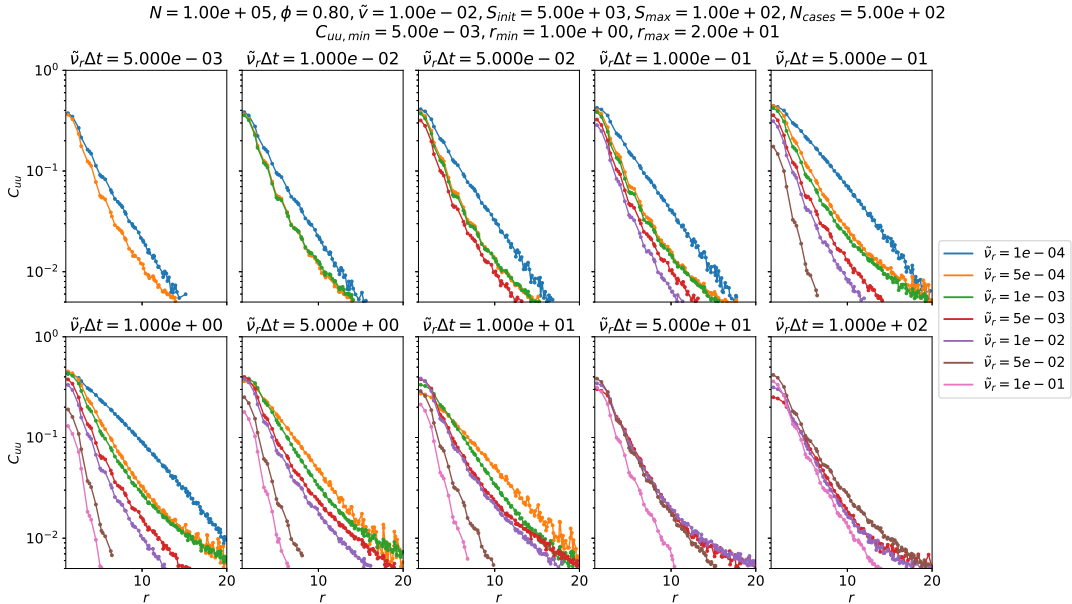


Figure 3.3: Comparison plot of displacement correlation functions $C_{uu}(r, \Delta t)$ as defined by equation 3.1, at packing fraction $\phi = 0.80$ and self-propelling velocity $\tilde{v} = 1 \cdot 10^{-2}$, for different values of the rotational diffusion rate \tilde{v}_r . Each panel corresponds to an unique value of the product $\tilde{v}_r \Delta t$.

We observe in figure 3.3 that for $\tilde{v}_r \Delta t < 1 \cdot 10^2$ we have $\forall r$ that the displacement correlation function at fixed $\tilde{v}_r \Delta t$, $C_{uu}(r, \tilde{v}_r \Delta t)$, is an increasing function of decreasing rotational diffusion rate \tilde{v}_r (*i.e.*, increasing

persistence time τ_r and Péclet number Pe). We thus have for low enough $\tilde{\nu}_r \Delta t$ that the spatial extent of the displacement correlation function increases with activity, which is what we expected from the analysis of figure 3.1.

However, we see for the highest value of $\tilde{\nu}_r \Delta t$ that this comparison becomes trickier. Curves actually cross, so what would be a correct definition of the "spatial extent" of the displacement correlation function which would be relevant in this case? Moreover, we stress that systematically comparing this amount of curves for each pair $(\phi, \tilde{\nu})$ and for all possible values of $\tilde{\nu}_r \Delta t$ is difficultly doable. We introduce in section 3.2 the cooperativity which should solve both these issues.

3.2 Cooperativity

3.2.1 Cooperativity

Inspired by [16, 36], we introduce the cooperativity, χ , linked to the displacement correlation, for a system within a square box of length L

$$\chi(\Delta t) = \frac{1}{L^2} \int_{r_{min}}^{r_{max}} dr 2\pi r C_{uu}(r, \Delta t) \quad (3.9)$$

with r_{min} close to the average particle separation a and r_{max} such that $C_{uu}(r > r_{max}, \Delta t)$ is negligible.

This quantity is a global measure of cooperative motion and represents the average proportion of particles acting as coherently moving neighbours [36]. It is thus a measure of the dynamic heterogeneity [37].

At short times, particles move independently of each others in their own cage, which leads to low displacement correlations $C_{uu}(r, \Delta t)$ and thus low cooperativity $\chi(\Delta t)$. As times increases, they feel the motion of their neighbours and displacements become correlated over an increasing length scale which leads to an increasing cooperativity. At high times, we expect the motion of two initially neighbouring particles to become uncorrelated, thus decreasing the cooperativity. We then expect the curves of $\chi(\Delta t)$ to be bell-shaped [16, 37]. The positions of their maxima will tell us about the time scales over which the motion of the particles is correlated, and their amplitudes about the number of particles involved in cooperative motion.

3.2.2 Varying rotational diffusion rate $\tilde{\nu}_r$

We have in figure 3.4 that $\chi(\Delta t)$ curves are indeed bell-shaped as we predicted.

For any lag time Δt , we have that the number of coherently moving neighbours is an increasing function of increasing activity (*i.e.*, increasing persistence time τ_r and Péclet number Pe , and decreasing rotational diffusion rate $\tilde{\nu}_r$). Moreover, we have

- that the maximum number of coherently moving neighbours, $\chi(\Delta t^*)$, is a strictly increasing function of the activity, indicating that dynamic heterogeneities grow as the activity grows,
- and that the lag time at which this maximum cooperative motion occurs, Δt^* , is also a strictly increasing function of the activity, which is consistent with the physical intuition that a cooperative behaviour involving a greater number of particles must happen at over a greater time scale.

We also note that there is a clear transition at $\text{Pe}_t \approx 10^{1.5}$ between two regimes wherein the increases of both Δt^* and $\chi(\Delta t^*)$ are algebraic in Pe and with different slopes. This transition value of the Péclet number is consistent with the approximate transition value between the fluid states and the phase separated states inferred from the local packing fraction histogram in figure 2.6.

We observe in figure 3.5 that for $\tilde{\nu}_r \Delta t \lesssim 10^2$, $\chi(\tilde{\nu}_r \Delta t)$, *i.e.* the number of coherently moving neighbours, is an increasing function of the activity, which is consistent with what we had observed in figure 3.1.

We have seen in section 1.1.3 that the persistence time τ_r qualitatively represents the amount of time during which the self-propelling velocity of particles remains oriented in the same direction. Thus, $\tilde{\nu}_r \Delta t = \Delta t / \tau_r$ represents the number of reorientations of this self-propelling velocity. We have in figure 3.5 that this number of reorientations corresponding to the time scale of maximum cooperativity, $\tilde{\nu}_r \Delta t^*$, is roughly a decreasing function of the Péclet number Pe for $\text{Pe} \lesssim \text{Pe}_t$ and an increasing function of Pe for $\text{Pe} \gtrsim \text{Pe}_t$, and is therefore

$$N = 1.0e + 05, \phi = 0.80, \tilde{v} = 1.00e - 02, r_{min} = 1.00e + 00, r_{max} = 2.00e + 01$$

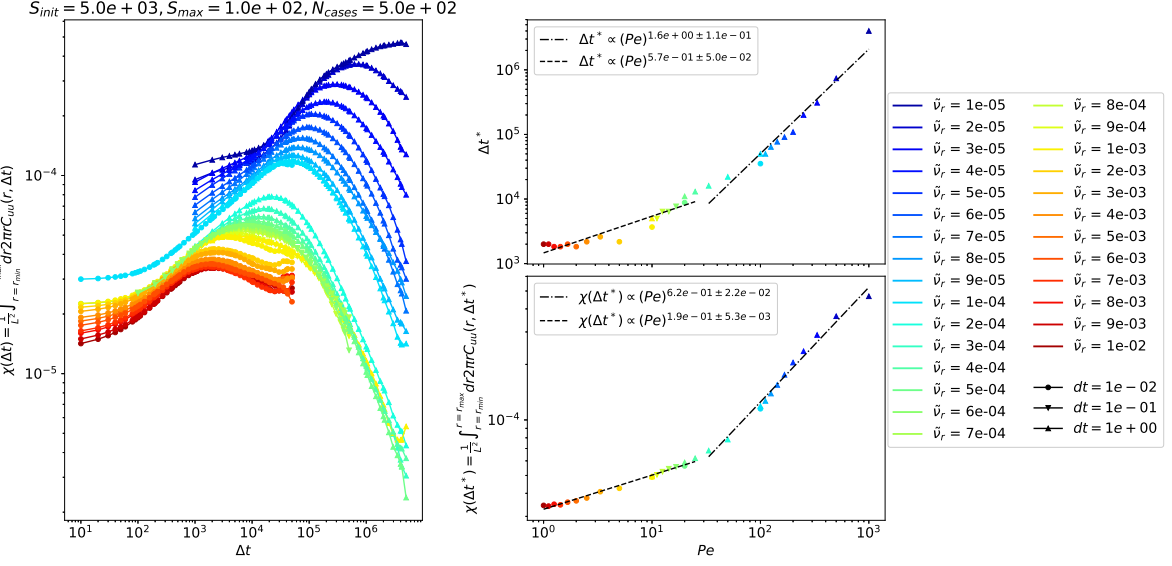


Figure 3.4: Cooperativities $\chi(\Delta t)$ as defined by equation 3.9, at packing fraction $\phi = 0.80$ and self-propelling velocity $\tilde{v} = 1 \cdot 10^{-2}$, for different values of the rotational diffusion rate \tilde{v}_r . Quantity dt refers to the time step used in the simulation. (**left**) Cooperativity as a function of lag time $\chi(\Delta t)$. Each continuous line corresponds to a single simulation. (**top right**) Position Δt^* of maximum cooperativity $\chi(\Delta t^*)$ as a function of the Péclet number $Pe = \tilde{v}/\tilde{v}_r$. Dashed lines correspond to arbitrary power law fits. (**bottom right**) Amplitude $\chi(\Delta t^*)$ of maximum cooperativity as a function of the Péclet number $Pe = \tilde{v}/\tilde{v}_r$. Dashed lines correspond to arbitrary power law fits.

$$N = 1.0e + 05, \phi = 0.80, \tilde{v} = 1.00e - 02, r_{min} = 1.00e + 00, r_{max} = 2.00e + 01$$

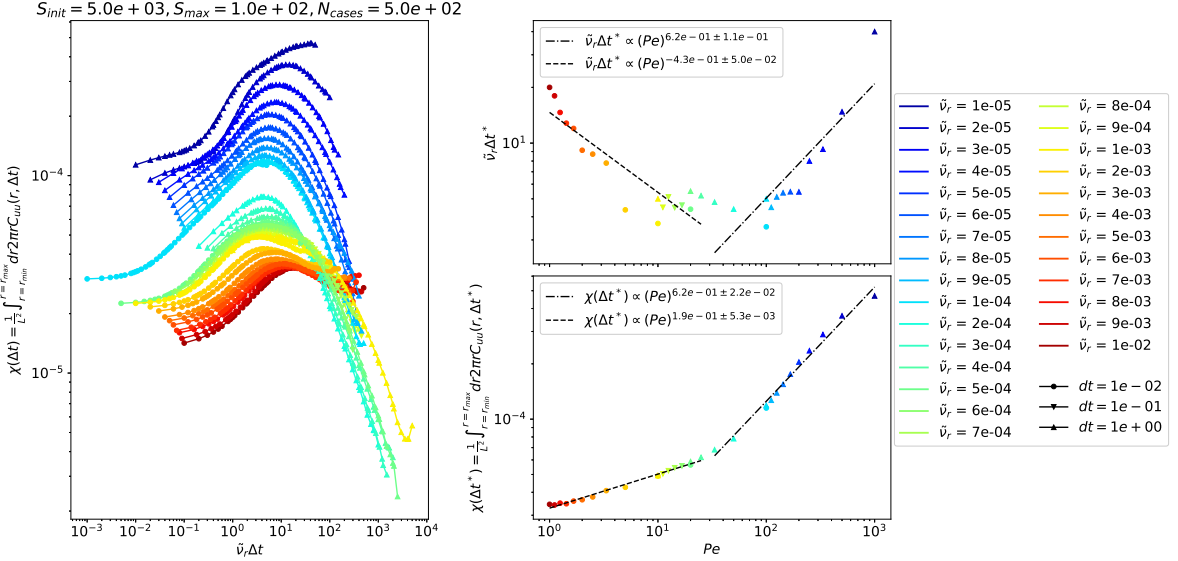


Figure 3.5: Cooperativities $\chi(\Delta t)$ as defined by equation 3.9, at packing fraction $\phi = 0.80$ and self-propelling velocity $\tilde{v} = 1 \cdot 10^{-2}$, for different values of the rotational diffusion rate \tilde{v}_r . Quantity dt refers to the time step used in the simulation. (**left**) Cooperativity as a function of the product of lag time and rotational diffusion rate $\chi(\tilde{v}_r \Delta t)$. Each continuous line corresponds to a single simulation. (**top right**) Position $\tilde{v}_r \Delta t^*$ of maximum cooperativity $\chi(\tilde{v}_r \Delta t^*)$ as a function of the Péclet number $Pe = \tilde{v}/\tilde{v}_r$. Dashed lines correspond to arbitrary power law fits. (**bottom right**) Amplitude $\chi(\Delta t^*)$ of maximum cooperativity as a function of the Péclet number $Pe = \tilde{v}/\tilde{v}_r$. Dashed lines correspond to arbitrary power law fits.

minimum at the transition value Pe_t . The origin of this behaviour is still an open question for us.

The quickly increasing dynamic heterogeneity, as measured by the maximum cooperativity $\chi(\Delta t^*)$, with increasing activity in the phase separated regime is reminiscent of the behaviour of a glass-forming material when decreasing its temperature [33, 37]. We can then look for other evidence of such behaviour, *e.g.* by looking at the mean square displacement as we have done in section 2.1.3 (figure 2.2).

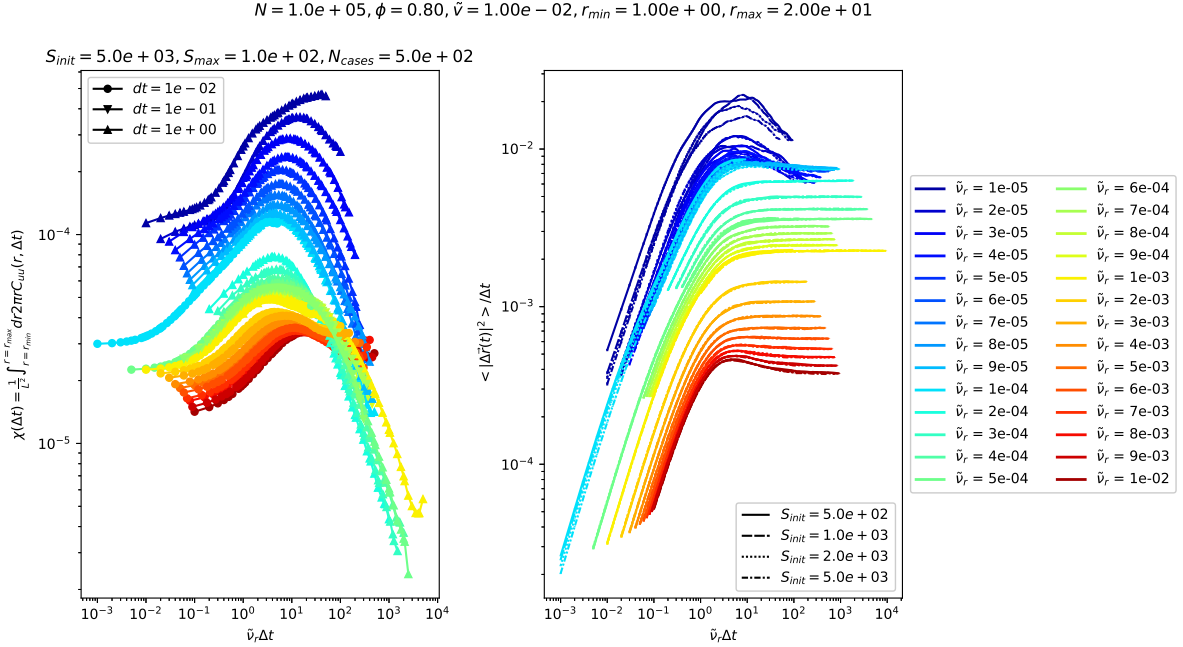


Figure 3.6: Cooperativities $\chi(\Delta t)$ as defined by equation 3.9, and mean square displacements as defined by equation 1.8, at packing fraction $\phi = 0.80$ and self-propelling velocity $\tilde{v} = 1 \cdot 10^{-2}$, for different values of the rotational diffusion rate $\tilde{\nu}_r$. Quantity dt refers to the time step used in the simulation. (**left**) Cooperativity as a function of the product of lag time and rotational diffusion rate $\chi(\tilde{\nu}_r \Delta t)$. Each continuous line corresponds to a single simulation. (**right**) Ratio of mean square displacement $\langle |\Delta \vec{r}(\Delta t)|^2 \rangle$ and lag time Δt as a function of lag time Δt . S_{init} refers to the frame of the simulation considered as the time $t = 0$ to compute mean square displacements.

We have in figure 3.6 that, for $\text{Pe} \lesssim \text{Pe}_t$, $\lim_{t \rightarrow +\infty} \langle |\Delta \vec{r}(t)|^2 \rangle = \text{cst}$, indicating a diffusive behaviour at high times which is what we would expect for fluid states [32]. For $\text{Pe} \gtrsim \text{Pe}_t$, there is a clear – and possibly transient – subdiffusive behaviour, such as observed in glasses, as we discussed in section 2.1.3.

An other evidence of glassiness is ageing [38], as illustrated by the dependence of mean square displacement curves $\langle |\Delta \vec{r}(t)|^2 \rangle$ with the simulation frame considered as initial in their calculation S_{init} .

3.2.3 Varying self-propelling velocity \tilde{v}

Figure 3.7 presents the few results we have so far for the cooperativity at fixed $(\phi, \tilde{\nu}_r)$ and varying self-propelling velocity \tilde{v} . Despite the great dispersion of the values of the number of reorientations corresponding to the time scale of maximum cooperativity $\tilde{\nu}_r \Delta t^*$ around our power law fits, we hypothesise that there is a transition at $\text{Pe} \approx 2 \cdot 10^2$ between regimes of decreasing and increasing $\tilde{\nu}_r \Delta t^*$ with increasing Pe , respectively for $\text{Pe} \lesssim \text{Pe}_t$ and $\text{Pe} \gtrsim \text{Pe}_t$. We first note that this transition value Pe of the Péclet number is consistent with the approximate transition value between the fluid states and the phase separated states inferred from the local packing fraction histogram in figure 2.5. We then highlight that this non-monotonous behaviour of $\tilde{\nu}_r \Delta t^*(\text{Pe})$ is similar to what has been observed when transitioning from the fluid regime to the phase separated regime by varying the rotational diffusion rate $\tilde{\nu}_r$ (see figure 3.5).

We also see in figure 3.7 that the maximum number of coherently moving neighbours, $\chi(\Delta t^*)$ is a strictly decreasing function of increasing Péclet number Pe . This is not only the exact opposite behaviour that what

$$N = 1.0e + 05, \phi = 1.00, \tilde{\nu}_r = 3.00e - 04, r_{min} = 1.00e + 00, r_{max} = 2.00e + 01$$

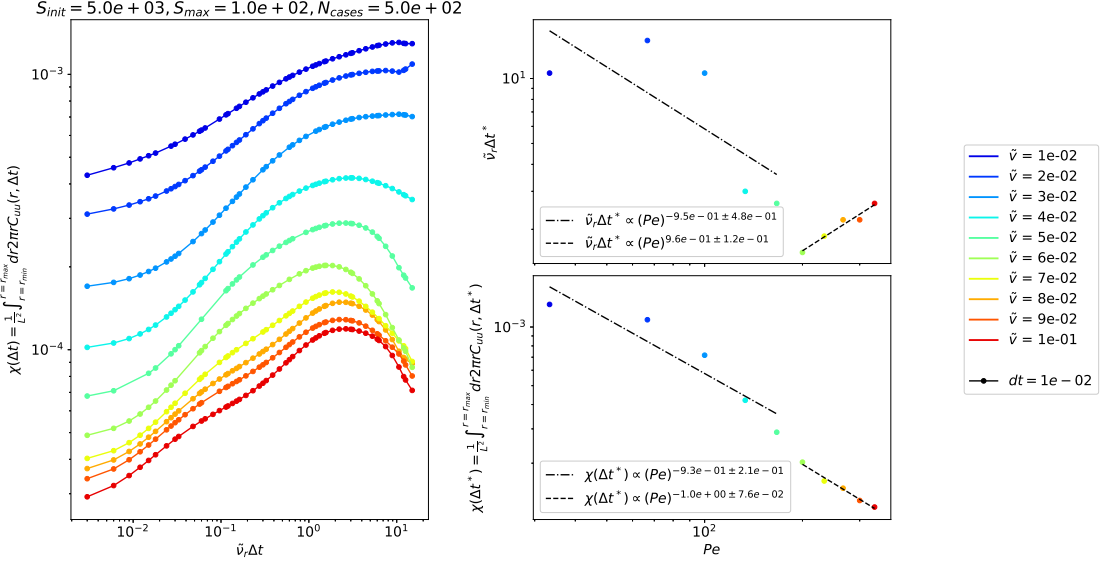


Figure 3.7: Cooperativities $\chi(\Delta t)$ as defined by equation 3.9, at packing fraction $\phi = 1.00$ and rotational diffusion rate $\tilde{\nu}_r = 3 \cdot 10^{-4}$, for different values of the self-propelling velocity $\tilde{\nu}$. Quantity dt refers to the time step used in the simulation. **(left)** Cooperativity as a function of the product of lag time and rotational diffusion rate $\chi(\tilde{\nu}_r \Delta t)$. Each continuous line corresponds to a single simulation. **(top right)** Position $\tilde{\nu}_r \Delta t^*$ of maximum cooperativity $\chi(\tilde{\nu}_r \Delta t^*)$ as a function of the Péclet number $Pe = \tilde{\nu}/\tilde{\nu}_r$. Dashed lines correspond to arbitrary power law fits. **(bottom right)** Amplitude $\chi(\Delta t^*)$ of maximum cooperativity as a function of the Péclet number $Pe = \tilde{\nu}/\tilde{\nu}_r$. Dashed lines correspond to arbitrary power law fits.

$$N = 1.0e + 05, \phi = 1.00, \tilde{\nu}_r = 3.00e - 04, r_{min} = 1.00e + 00, r_{max} = 2.00e + 01$$

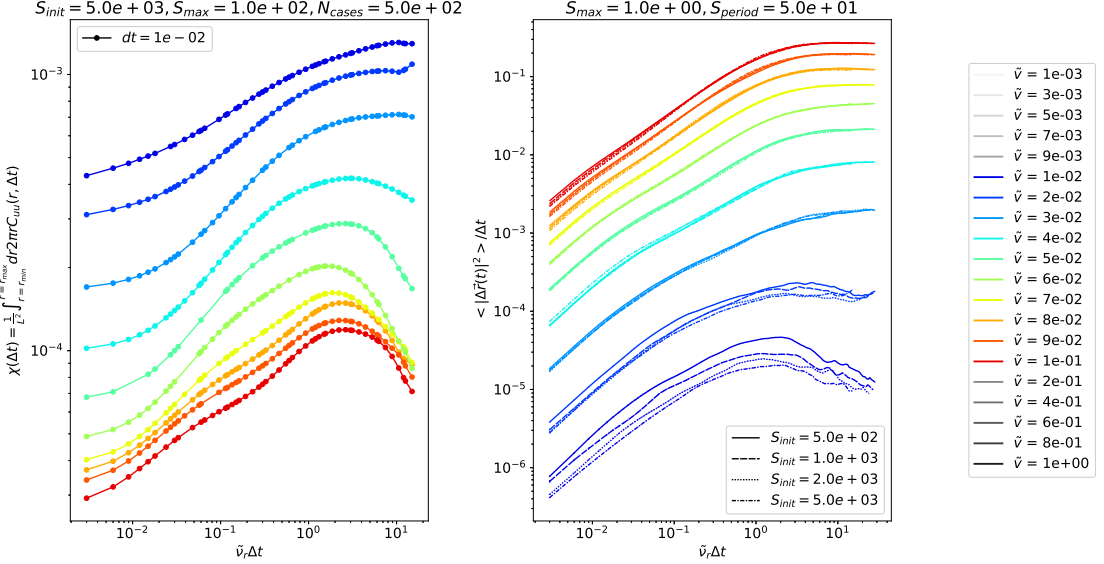


Figure 3.8: Cooperativities $\chi(\Delta t)$ as defined by equation 3.9, and mean square displacements as defined by equation 1.8, at packing fraction $\phi = 1.00$ and rotational diffusion rate $\tilde{\nu}_r = 3 \cdot 10^{-4}$, for different values of the self-propelling velocity $\tilde{\nu}$. Quantity dt refers to the time step used in the simulation. **(left)** Cooperativity as a function of the product of lag time and rotational diffusion rate $\chi(\tilde{\nu}_r \Delta t)$. Each continuous line corresponds to a single simulation. **(right)** Ratio of mean square displacement $\langle |\Delta \vec{r}(\Delta t)|^2 \rangle$ and lag time Δt as a function of lag time Δt . S_{init} refers to the frame of the simulation considered as the time $t = 0$ to compute mean square displacements.

was observed when varying the rotational diffusion rate $\tilde{\nu}_r$ (see figure 3.5), this is also quite counter intuitive. Indeed, we remind that the Péclet number represents the dimensionless distance travelled by a single particle before its self-propulsion orientation decorrelates. We would then expect that the greater this number is, the larger the cluster of coherently moving neighbours get. The origin of this behaviour is still an open question for us.

What is however clear from these findings is that the sole Péclet number Pe is not enough to characterise our model system, contrarily to what has been considered in [16].

We observe in figure 3.8 both subdiffusive and ageing behaviours in mean square displacements for $\tilde{v} = 1 \cdot 10^{-2}, 2 \cdot 10^{-2}$. This is consistent with the positions of these points in the phase diagram of figure 2.3 where they sit in the "frozen" states.

However, we see for the highest values of the self-propelling velocity \tilde{v} (*i.e.*, for the highest values of the Péclet number Pe) that the mean square displacements show no sign of either subdiffusive or ageing behaviours, even though we had observed it for $\text{Pe} \gtrsim \text{Pe}_t$ when varying the rotational diffusion rate $\tilde{\nu}_r$ (see figure 3.6).

Maybe the reason to this is that we are not deep enough in the phase separated regime. We hypothesise that, for higher values of the self-propelling velocity \tilde{v} , the dynamic heterogeneity as measured by the maximum number of coherently moving neighbours $\chi(\Delta t^*)$ would eventually increase.

3.3 Directional displacement correlation

3.3.1 Directional displacement correlation

Definition

We have seen the influence of activity on the cooperativity of the motion of particles as measured by the spatial extent of displacement correlation functions (section 3.2). We can now wonder if activity affects the correlations in the directions of motion of pairs of particles.

To this effect, we introduce the longitudinal and transversal displacement correlations [34, 39]

$$\begin{aligned} C_{uu}^L(\Delta\vec{r}, \Delta t) &= \langle u_L(\vec{r} + \Delta\vec{r}, t, t + \Delta t) u_L(\vec{r}, t, t + \Delta t) \rangle_{\vec{r}, t} \\ C_{uu}^T(\Delta\vec{r}, \Delta t) &= \langle \vec{u}_T(\vec{r} + \Delta\vec{r}, t, t + \Delta t) \cdot \vec{u}_T(\vec{r}, t, t + \Delta t) \rangle_{\vec{r}, t} \end{aligned} \quad (3.10)$$

with $u_L(\vec{r}, t, t + \Delta t)$ the longitudinal displacement and $\vec{u}_T(\vec{r}, t, t + \Delta t)$ the transversal displacement, defined as

$$\vec{u}(\vec{r}, t, t + \Delta t) = \underbrace{\frac{\vec{u}(\vec{r}, t, t + \Delta t) \cdot \Delta\vec{r}}{||\Delta\vec{r}||}}_{u_L(\vec{r}, t, t + \Delta t)} \frac{\Delta\vec{r}}{||\Delta\vec{r}||} + \underbrace{\vec{u}(\vec{r}, t, t + \Delta t) - u_L(\vec{r}, t, t + \Delta t)\Delta\vec{r}}_{\vec{u}_T(\vec{r}, t, t + \Delta t) \perp \Delta\vec{r}} \quad (3.11)$$

where $\vec{u}(\vec{r}, t, t + \Delta t)$ is the displacement vector of the particle at position \vec{r} at time t between times t and $t + \Delta t$.

We are interested in the correlations in the directions of motion of pairs of *neighbouring* particles, we will then only consider the values of the transversal and longitudinal displacement correlations at a fixed radius close to the interparticle distance $r \approx a$ in equation 3.10. Without further notice, we will use functions $C_{uu}^L(\Delta t)$ and $C_{uu}^T(\Delta t)$ of the sole lag time Δt .

Computation details

Longitudinal and transversal displacement correlations are calculated with the same routine as displacement correlations (see section 3.1.2). Our computation script is available at [yketa/active_particles/analysis/cuu.py](#).

Raw data with varying rotational diffusion rate $\tilde{\nu}_r$

We have that data in figure 3.9 is difficultly exploitable. $C_{uu}^L(\tilde{\nu}_r \Delta t)$ and $C_{uu}^T(\tilde{\nu}_r \Delta t)$ are non-monotonous and is hard to establish whether any of these approach a limiting curve in either low or high rotational diffusion rate $\tilde{\nu}_r$ limit.

Values of $C_{uu}^L(\Delta t^*)$ and $C_{uu}^T(\Delta t^*)$ for $\text{Pe} \lesssim 10^1$ look well behaved and are an increasing function of the Péclet number for the former and more or less constant for the latter. However, for $\text{Pe} > 10^1$, it becomes trickier to make any assertion about the behaviour of these quantities.

We then propose to look not at the raw values of the longitudinal and transversal displacement correlations but at their ratio, as was done in [39].

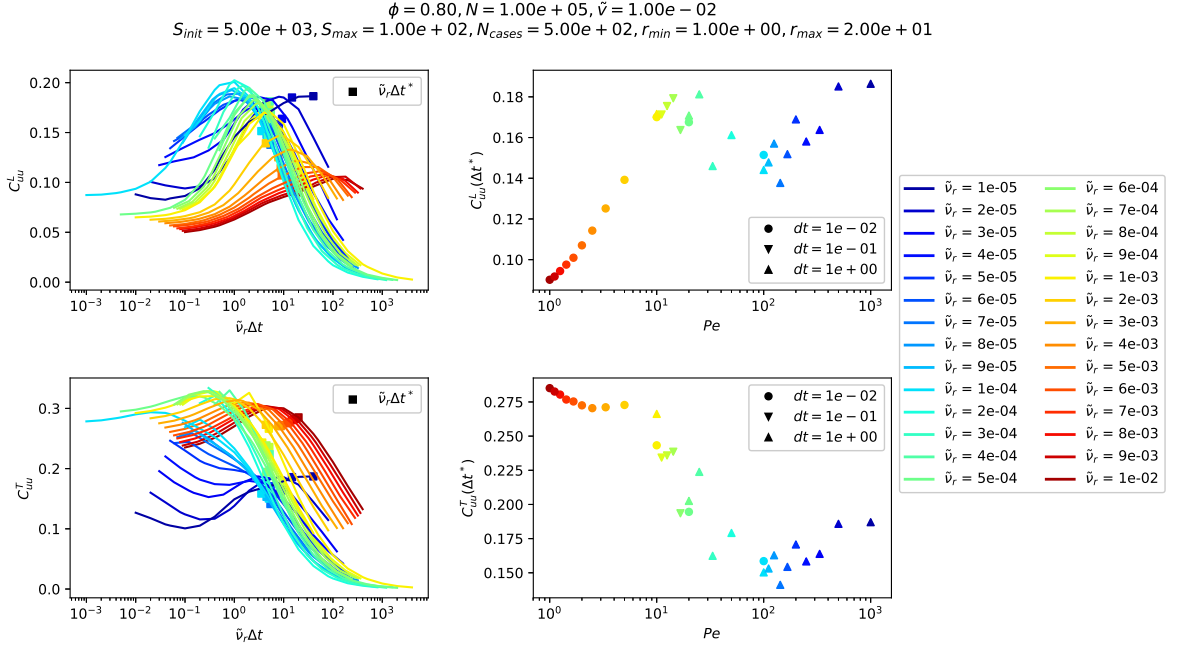


Figure 3.9: Longitudinal and transversal displacement correlations as defined by equation 3.10, at packing fraction $\phi = 0.80$ and self-propelling velocity $\tilde{v} = 1 \cdot 10^{-2}$, for different values of the rotational diffusion rate $\tilde{\nu}_r$. **(left)** Longitudinal (top) and transversal (bottom) displacement correlations as functions of the product of the rotational diffusion rate $\tilde{\nu}_r$ and the lag time Δt . Square markers mark the number of reorientations corresponding to the time scale of maximum cooperativity $\tilde{\nu}_r \Delta t^*$ (see figure 3.5). Each continuous line corresponds to a single simulation. **(right)** Longitudinal (top) and transversal (bottom) displacement correlations at times of maximum cooperativity as functions of the Péclet number $\text{Pe} = \tilde{v}/\tilde{\nu}_r$. Quantity dt refers to the time step used in the simulation.

3.3.2 Varying rotational diffusion rate $\tilde{\nu}_r$

We see in figure 3.10 that the ratio of transversal and longitudinal displacement correlations $C_{uu}^T/C_{uu}^L(\Delta t)$ is better behaved than the separated functions (figure 3.9).

We observe that

- at low times, this ratio has a plateau which value is greater than 1 and increases with increasing rotational diffusion rate $\tilde{\nu}_r$ (*i.e.*, decreasing persistence time τ_r and Péclet number Pe) ;
- at high times, this ratio is constant and equal to 1.

We expect the limit $\lim_{\Delta t \rightarrow +\infty} C_{uu}^T/C_{uu}^L(\Delta t) = 1$ to come from the decorrelation of the displacements of the particles at high lag times. There is no correlation in the directions of motion of pairs of particles, thus the transversal and longitudinal displacement correlations must be equal.

Looking at the values of the ratio at the lag time of maximum cooperativity, we note that there is a clear transition at $\text{Pe}_t \approx 10^{1.5}$ between a regime where $C_{uu}^T/C_{uu}^L(\Delta t^*) > 1$ for $\text{Pe} < \text{Pe}_t$ and a regime where $C_{uu}^T/C_{uu}^L(\Delta t^*) \approx 1$ for $\text{Pe} > \text{Pe}_t$. We note that this transition value of the Péclet number is consistent with the approximate transition value between the fluid states and the phase separated states inferred from the local

packing fraction histogram in figure 2.6, and with the transition value found in cooperativity plots in figure 3.4.

We had observed in displacement maps at high activity (see figure 3.1) that neighbouring particles form blocks of similar displacements, both in amplitude and direction. It follows that for these coherently moving particles, longitudinal and transversal displacement correlations are equal. This is why the value of the ratio of these correlations is equal to 1 at lag times of maximum cooperativity in the phase separated regime.

In the fluid regime, figure 3.10 shows that displacements are mostly correlated in the transverse directions of lines joining pairs of particles.

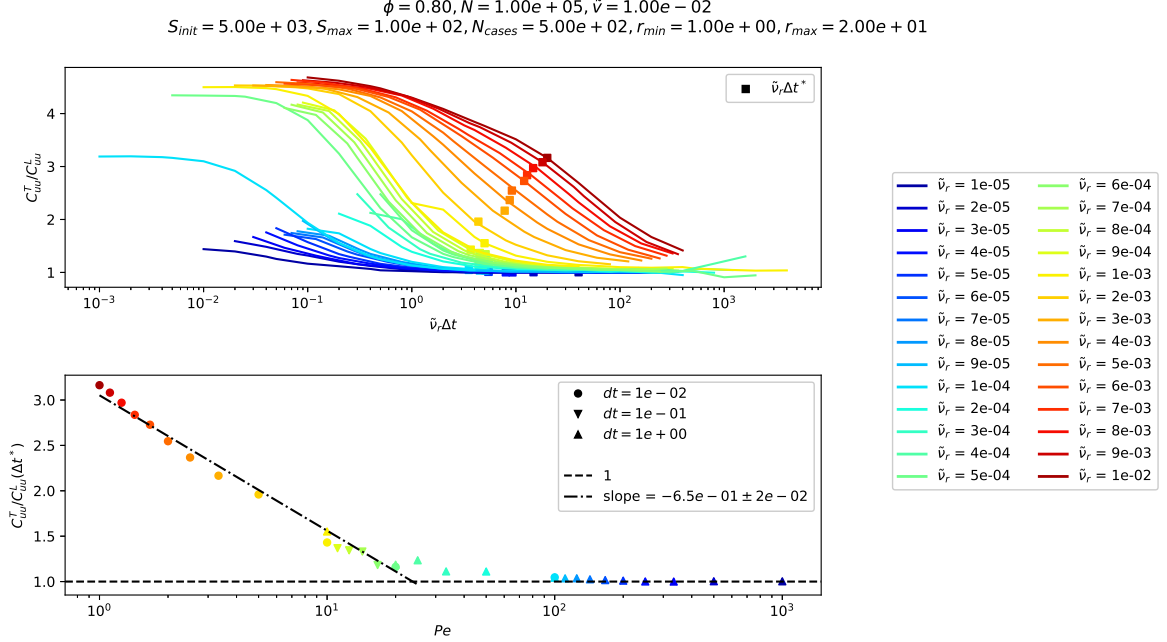


Figure 3.10: Ratio of transversal and longitudinal displacement correlations as defined by equation 3.10, at packing fraction $\phi = 0.80$ and self-propelling velocity $\tilde{v} = 1 \cdot 10^{-2}$, for different values of the rotational diffusion rate $\tilde{\nu}_r$. **(top)** Ratio of transversal and longitudinal displacement correlations as function of the product of the rotational diffusion rate $\tilde{\nu}_r$ and the lag time Δt . Square markers mark the number of reorientations corresponding to the time scale of maximum cooperativity $\tilde{\nu}_r \Delta t^*$ (see figure 3.5). Each continuous line corresponds to a single simulation. **(bottom)** Ratio of transversal and longitudinal displacement correlations at lag time of maximum cooperativity Δt^* as function of the Péclet number $Pe = \tilde{v}/\tilde{\nu}_r$. Dash-dotted line correspond to an arbitrary logarithm fit, and dashed line to $C_{uu}^T/C_{uu}^L(\Delta t^*) = 1$.

3.3.3 Varying self-propelling velocity \tilde{v}

We observe in figure 3.11 that

- at low times, the ratio of transversal and longitudinal displacement correlations has a plateau which value is greater than 1 and increases with increasing self-propelling velocity \tilde{v} (*i.e.*, increasing Péclet number Pe) ;
- at high times, this ratio is constant and equal to 1.

However, compared to the case of fixed (ϕ, \tilde{v}) and varying rotational diffusion rate $\tilde{\nu}_r$ (see figure 3.10), we now have that the value of the ratio at the time of maximum cooperativity Δt^* is more or less constant and equal to 1 for all values of the self-propelling velocity \tilde{v} . There is thus no effect of the transition from the fluid regime to the phase separated regime in this particular case.

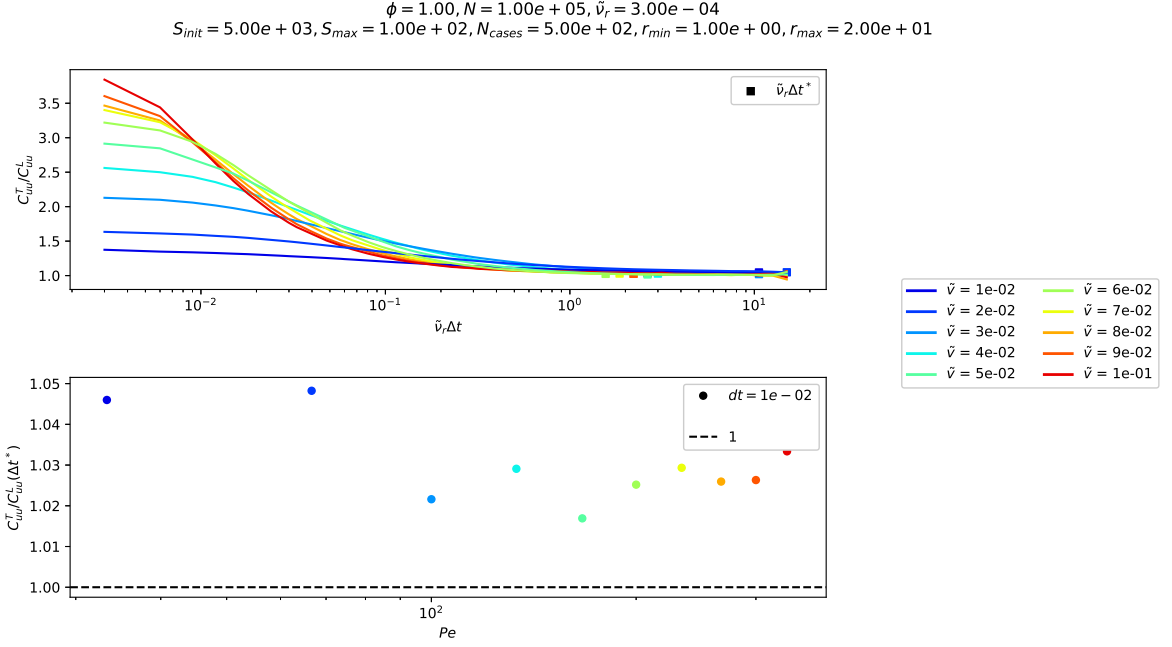


Figure 3.11: Ratio of transversal and longitudinal displacement correlations as defined by equation 3.10, at packing fraction $\phi = 1.00$ and rotational diffusion rate $\tilde{\nu}_r = 3 \cdot 10^{-4}$, for different values of the self-propelling velocity $\tilde{\nu}$. **(top)** Ratio of transversal and longitudinal displacement correlations as function of the product of the rotational diffusion rate $\tilde{\nu}_r$ and the lag time Δt . Square markers mark the number of reorientations corresponding to the time scale of maximum cooperativity $\tilde{\nu}_r \Delta t^*$ (see figure 3.5). Each continuous line corresponds to a single simulation. **(bottom)** Ratio of transversal and longitudinal displacement correlations at lag time of maximum cooperativity Δt^* as function of the Péciel number $Pe = \tilde{\nu}/\tilde{\nu}_r$. Dash-dotted line correspond to an arbitrary logarithm fit, and dashed line to $C_{uu}^T/C_{uu}^L(\Delta t^*) = 1$.

3.4 Overview

We present here comparison plots of the quantities we have introduced for the two paths in the phase diagram we have studied:

- (i) $(\phi = 0.80, \tilde{\nu} = 1 \cdot 10^{-2}, \tilde{\nu}_r = 1 \cdot 10^{-5} \rightarrow 1 \cdot 10^{-2})$ (figure 3.12)
- (ii) $(\phi = 1.00, \tilde{\nu} = 1 \cdot 10^{-2} \rightarrow 1 \cdot 10^{-1}, \tilde{\nu}_r = 3 \cdot 10^{-4})$ (figure 3.13)

These plots highlight how

- (i) the most probable local packing fraction ϕ_{loc}^* ,
- (ii) the maximum cooperativity $\chi(\Delta t^*)$,
- (iii) the number of reorientations corresponding to the time scale of maximum cooperativity $\tilde{\nu}_r \Delta t^*$,
- (iv) and the ratio of transversal and longitudinal displacement correlations at maximum cooperativity $C_{uu}^T/C_{uu}^L(\Delta t^*)$ (only in the case of figure 3.12),

all enable us to spot the transition between fluid and phase separated regimes.

3.4.1 Varying rotational diffusion rate $\tilde{\nu}_r$

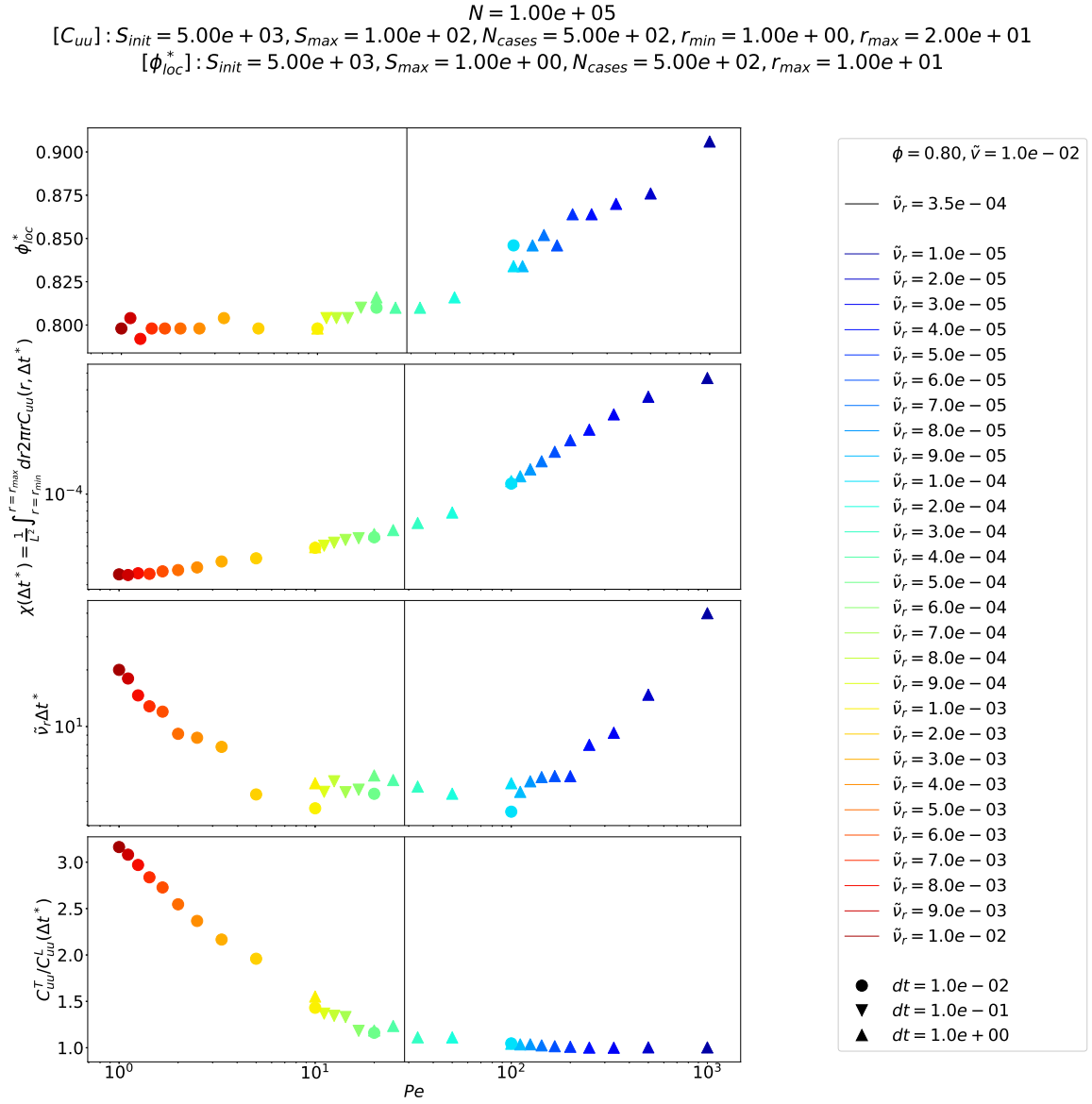


Figure 3.12: Comparison of (from top to bottom) most probable local packing fraction ϕ_{loc}^* (see section 2.2.1), maximum cooperativity $\chi(\Delta t^*)$ (see section 3.2), number of reorientations corresponding to the time scale of maximum cooperativity $\tilde{\nu}_r \Delta t^*$ (see section 3.2), and ratio of transversal and longitudinal displacement correlations at maximum cooperativity $C_{uu}^T/C_{uu}^L(\Delta t^*)$ (see section 3.3), as functions of the Péclet number $Pe = \tilde{v}/\tilde{\nu}_r$, at packing fraction $\phi = 0.80$ and self-propelling velocity $\tilde{v} = 1 \cdot 10^{-2}$. The vertical line corresponds to an arbitrarily chosen value of the transition Péclet number.

3.4.2 Varying self-propelling velocity \tilde{v}

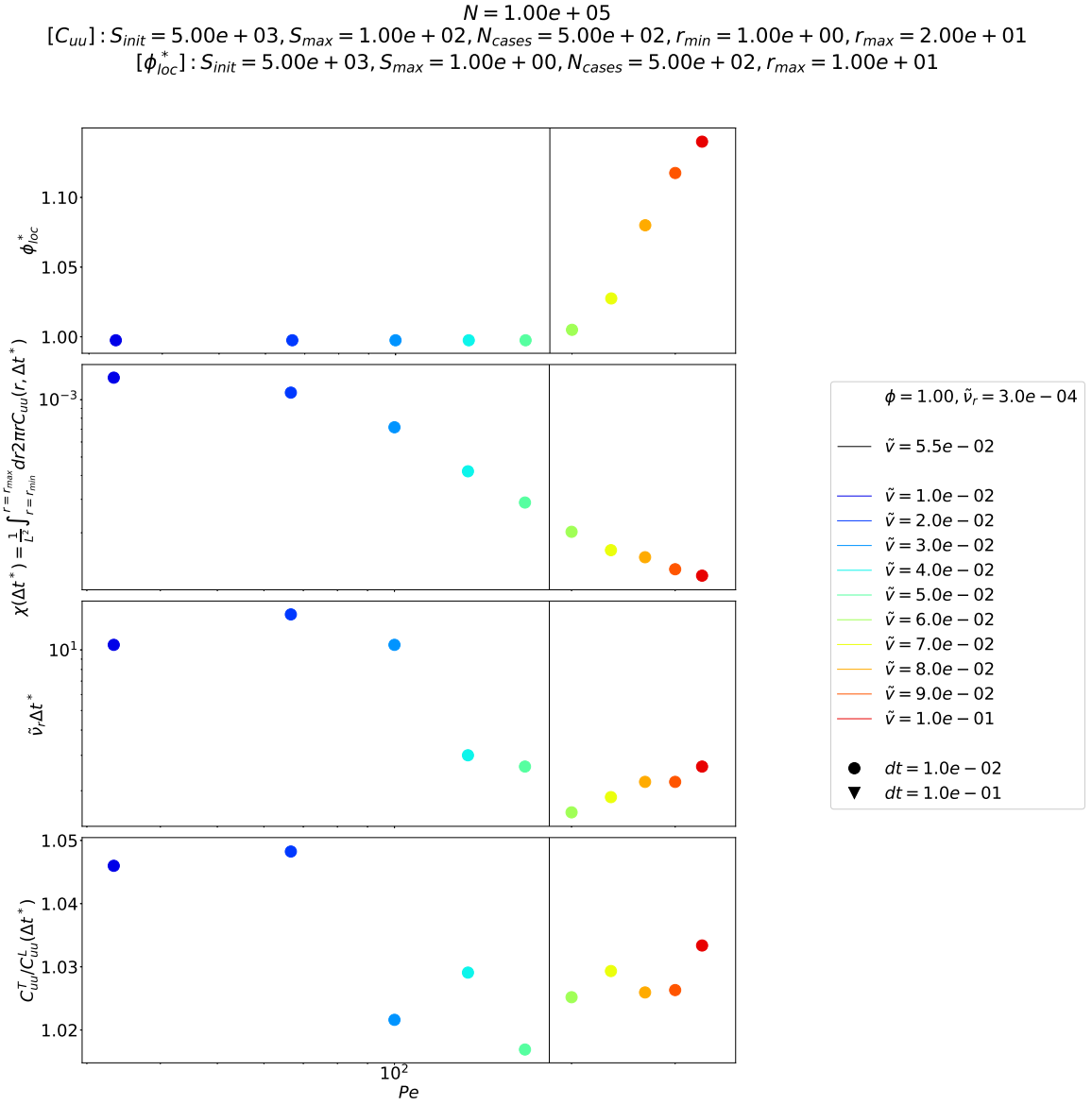


Figure 3.13: Comparison of (from top to bottom) most probable local packing fraction ϕ_{loc}^* (see section 2.2.1), maximum cooperativity $\chi(\Delta t^*)$ (see section 3.2), number of reorientations corresponding to the time scale of maximum cooperativity $\tilde{\nu}_r \Delta t^*$ (see section 3.2), and ratio of transversal and longitudinal displacement correlations at maximum cooperativity $C_{uu}^T / C_{uu}^L(\Delta t^*)$ (see section 3.3), as functions of the Péclet number $Pe = \tilde{v}/\tilde{\nu}_r$, at packing fraction $\phi = 1.00$ and rotational diffusion rate $\tilde{\nu}_r = 3 \cdot 10^{-4}$. The vertical line corresponds to an arbitrarily chosen value of the transition Péclet number.

4 | Shear strain correlation

4.1 Plastic deformation

Current theories of plastic deformation of amorphous solids rely on the existence of *shear transformation zones*, which are special sites, a few particles wide, where particles are able to rearrange themselves in response to applied stresses [40]. Plastic deformation is then the consequence of localized irreversible rearrangements, coupled by elastic strain fields [41] which are solutions of the Eshelby inclusion problem [42].

These plastic rearrangements, coupled in an elastic medium, have also been observed in supercooled liquids near the glass transition [43–45], hence the claim that supercooled liquids are "solids that flow" [46].

With $\varepsilon_{xy}(\vec{r}, t, t + \Delta t)$ the accumulated shear strain at position \vec{r} and between times t and $t + \Delta t$ (see section 4.2.1), we have in these systems that $C_{\varepsilon_{xy}\varepsilon_{xy}}(\Delta\vec{r}, \Delta t)$, its autocorrelation function (see section 4.2.2), has the same quadrupolar symmetry and algebraic decay far from the origin as the strain field [44, 45], *i.e.*

$$C_{\varepsilon_{xy}\varepsilon_{xy}}(\Delta\vec{r}, \Delta t) \underset{\substack{a \propto \\ ||\Delta\vec{r}|| \gg 1}}{\sim} \frac{\cos 4\theta}{||\Delta\vec{r}||^2} \quad (4.1)$$

in 2 dimensions, with a the average interparticle distance.

In this chapter, we aim at determining if the transition from the fluid to the phase separated regime is associated with the development of algebraic shear strain correlations.

4.2 Shear strain

4.2.1 Shear strain

With $\vec{u}(\vec{r}, t, t + \Delta t) = \begin{pmatrix} u_x(\vec{r}, t, t + \Delta t) \\ u_y(\vec{r}, t, t + \Delta t) \end{pmatrix}$ the displacement of particle at position \vec{r} at time t between times t and $t + \Delta t$, we introduce the linearised strain tensor $\bar{\varepsilon}$ [47]

$$\bar{\varepsilon}(\vec{r}, t, t + \Delta t) \underset{\frac{||\vec{u}||}{L} \ll 1}{=} \begin{pmatrix} \frac{\partial}{\partial x} u_x(\vec{r}, t, t + \Delta t) & \frac{1}{2} \left(\frac{\partial}{\partial y} u_x(\vec{r}, t, t + \Delta t) + \frac{\partial}{\partial x} u_y(\vec{r}, t, t + \Delta t) \right) \\ \frac{1}{2} \left(\frac{\partial}{\partial y} u_x(\vec{r}, t, t + \Delta t) + \frac{\partial}{\partial x} u_y(\vec{r}, t, t + \Delta t) \right) & \frac{\partial}{\partial y} u_y(\vec{r}, t, t + \Delta t) \end{pmatrix} \quad (4.2)$$

with L the characteristic length of the system, in which we will consider only the diagonal terms, *i.e.* the linearised shear strain

$$\varepsilon_{xy}(\vec{r}, t, t + \Delta t) = \varepsilon_{yx} = \frac{1}{2} \left(\frac{\partial}{\partial y} u_x(\vec{r}, t, t + \Delta t) + \frac{\partial}{\partial x} u_y(\vec{r}, t, t + \Delta t) \right) \quad (4.3)$$

which characterises the deformation of the system perpendicularly to the direction of deformation.

4.2.2 Shear strain correlation

We define the shear strain correlation, which is the auto-correlation function of the linearised shear strain introduced in equation 4.3

$$\begin{aligned} C_{\varepsilon_{xy}\varepsilon_{xy}}(\Delta\vec{r}, \Delta t) &= \langle \varepsilon_{xy}(\vec{r} + \Delta\vec{r}, t, t + \Delta t) \varepsilon_{xy}(\vec{r}, t, t + \Delta t) \rangle_{\vec{r}, t} \\ &= \frac{\int dt \int d^2\vec{r} \varepsilon_{xy}(\vec{r}, t, t + \Delta t) \varepsilon_{xy}(\vec{r} + \Delta\vec{r}, t, t + \Delta t)}{\int dt \int d^2\vec{r} |\varepsilon_{xy}(\vec{r}, t, t + \Delta t)|^2} \\ &= \frac{\mathcal{F}^{-1} \{ \int dt |\mathcal{F}\{\varepsilon_{xy}\}(\vec{k}, t, t + \Delta t)|^2 \} (\Delta\vec{r}, \Delta t)}{\int dt \int d^2\vec{r} ||\varepsilon_{xy}(\vec{r}, t, t + \Delta t)||^2} \end{aligned} \quad (4.4)$$

where we refer to appendix A.1 for calculation details leading to the last line of equation 4.4.

As discussed in section 4.1, we expect $C_{\varepsilon_{xy}\varepsilon_{xy}}(\Delta\vec{r}, \Delta t)$ to have a four-fold symmetry. Inspired by [44], we then introduce the projection of the shear strain correlation on $\cos 4\theta$

$$C_4^4(\Delta r, \Delta t) = \frac{1}{\pi} \int_0^{2\pi} d\theta \cos(4\theta) C_{\varepsilon_{xy}\varepsilon_{xy}}(\Delta\vec{r} \equiv (\Delta r, \theta), \Delta t) \quad (4.5)$$

which in a 2D elastic medium should decay algebraically far from the origin

$$C_4^4(\Delta r, \Delta t) \underset{\frac{\Delta r}{a} \gg 1}{\propto} \frac{1}{\Delta r^2} \quad (4.6)$$

where a is the average interparticle distance.

4.3 Real space method

4.3.1 Method

Coarse-graining

We only have access to discrete particle positions to calculate displacements. In order to obtain smooth strain fields, we then have to go through some sort of coarse-graining of these displacements.

On the basis of a method detailed in [48], we define the coarse-graining operator $\mathcal{A}(\sigma, r_c)$ which associates to any particle-dependent variable $c_i(t)$ its coarse-grained version $\bar{c}(\vec{r}, t)$ such that

$$\bar{c}(\vec{r}, t) = \mathcal{A}(\sigma, r_c)\{c_i(t)\} = \sum_{i=1}^N c_i(t) \phi(\vec{r} - \vec{r}_i(t), \sigma, r_c) \quad (4.7)$$

where $\phi(\vec{r}, \sigma, r_c)$ is a normalised non-negative coarse-graining function, with a single maximum at $\vec{r} = \vec{0}$, of width σ – the coarse-graining scale – and cut-off radius r_c .

As has been done in [44], we choose a Gaussian coarse-graining function $\phi(\vec{r}, \sigma, r_c)$ of width σ with a cut-off radius r_c

$$\phi(\vec{r}, \sigma, r_c) = \frac{1}{\mathcal{N}(\sigma, r_c)} \begin{cases} \exp\left(-\frac{||\vec{r}||^2}{2\sigma^2}\right) & \text{if } ||\vec{r}|| < r_c \\ 0 & \text{otherwise} \end{cases} \quad (4.8)$$

where $\mathcal{N}(\sigma, r_c)$ normalises the function, *i.e.* is such that

$$\int_{\mathbb{R}^2} d^2\vec{r} \phi(\vec{r}, \sigma, r_c) = \frac{1}{\mathcal{N}(\sigma, r_c)} \int_0^{r_c} dr 2\pi r \exp\left(-\frac{r^2}{2\sigma^2}\right) = 1 \Leftrightarrow \mathcal{N}(\sigma, r_c) = 2\pi\sigma^2 \left(1 - \exp\left(-\frac{r_c^2}{2\sigma^2}\right)\right) \quad (4.9)$$

It is straightforward to verify that this coarse-graining function satisfies the aforementioned conditions.

We then define the coarse-grained displacement field [44]

$$\bar{u}(\vec{r}, t, t + \Delta t) = \frac{1}{\bar{\rho}(\vec{r}, t)} \mathcal{A}(\sigma, r_c)\{\bar{u}(\vec{r}_i(t), t, t + \Delta t)\} = \frac{1}{\bar{\rho}(\vec{r}, t)} \sum_{i=1}^N \bar{u}(\vec{r}_i(t), t, t + \Delta t) \phi(\vec{r} - \vec{r}_i(t), \sigma, r_c) \quad (4.10)$$

where $\bar{\rho}(\vec{r}, t)$ is the coarse-grained density

$$\bar{\rho}(\vec{r}, t) = \mathcal{A}(\sigma, r_c)\{m_i\} = \sum_{i=1}^N m_i \phi(\vec{r} - \vec{r}_i(t), \sigma, r_c) \quad (4.11)$$

with m_i the mass of particle i .

It follows, from equations 4.3 and 4.10, the expression of the linearised shear strain from the coarse-grained displacements

$$\begin{aligned}
\varepsilon_{xy}(\vec{r}, t, t + \Delta t) &= \frac{1}{2} \left(\frac{\partial}{\partial x} \bar{u}_y(\vec{r}, t, t + \Delta t) + \frac{\partial}{\partial y} \bar{u}_x(\vec{r}, t, t + \Delta t) \right) \\
&= \frac{1}{2} \left[\frac{\partial}{\partial x} \left(\frac{1}{\bar{\rho}(\vec{r}, t)} \right) \sum_{i=1}^N u_y(\vec{r}_i(t), t, t + \Delta t) \phi(\vec{r} - \vec{r}_i(t), \sigma, r_c) \right. \\
&\quad \underbrace{\mathcal{A}(\sigma, r_c) \{u_y(\vec{r}_i(t), t, t + \Delta t)\}}_{\mathcal{A}(\sigma, r_c) \{u_y(\vec{r}_i(t), t, t + \Delta t)\}} \\
&\quad + \frac{1}{\bar{\rho}(\vec{r}, t)} \sum_{i=1}^N u_y(\vec{r}_i(t), t, t + \Delta t) \frac{\partial}{\partial x} (\phi(\vec{r} - \vec{r}_i(t), \sigma, r_c)) \\
&\quad + \frac{\partial}{\partial y} \left(\frac{1}{\bar{\rho}(\vec{r}, t)} \right) \sum_{i=1}^N u_x(\vec{r}_i(t), t, t + \Delta t) \phi(\vec{r} - \vec{r}_i(t), \sigma, r_c) \\
&\quad \underbrace{\mathcal{A}(\sigma, r_c) \{u_x(\vec{r}_i(t), t, t + \Delta t)\}}_{\mathcal{A}(\sigma, r_c) \{u_x(\vec{r}_i(t), t, t + \Delta t)\}} \\
&\quad \left. + \frac{1}{\bar{\rho}(\vec{r}, t)} \sum_{i=1}^N u_x(\vec{r}_i(t), t, t + \Delta t) \frac{\partial}{\partial x} (\phi(\vec{r} - \vec{r}_i(t), \sigma, r_c)) \right] \tag{4.12}
\end{aligned}$$

where we have, $\forall \vec{r}$ such that $\|\vec{r}\| < r_c$,

$$\begin{aligned}
\frac{\partial}{\partial \vec{r}} \phi(\vec{r} - \vec{r}_i(t), \sigma, r_c) &= \frac{1}{\mathcal{N}(\sigma, r_c)} \frac{\partial}{\partial \vec{r}} \exp \left(-\frac{\|\vec{r} - \vec{r}_i(t)\|^2}{2\sigma^2} \right) \\
&= -\frac{\vec{r} - \vec{r}_i(t)}{\mathcal{N}(\sigma, r_c) \sigma^2} \exp \left(-\frac{\|\vec{r} - \vec{r}_i(t)\|^2}{2\sigma^2} \right) \\
&= -\frac{\vec{r} - \vec{r}_i(t)}{\sigma^2} \phi(\vec{r} - \vec{r}_i(t), \sigma, r_c)
\end{aligned} \tag{4.13}$$

which result can be extrapolated to any \vec{r} , and from which it directly follows for any particle-dependent variable $c_i(t)$ that

$$\begin{aligned}
\frac{\partial}{\partial \vec{r}} \bar{c}(\vec{r}, t) &= \sum_{i=1}^N c_i(t) \frac{\partial}{\partial \vec{r}} \phi(\vec{r} - \vec{r}_i(t), \sigma, r_c) \\
&= -\frac{1}{\sigma^2} \sum_{i=1}^N c_i(t) (\vec{r} - \vec{r}_i(t)) \phi(\vec{r} - \vec{r}_i(t), \sigma, r_c) \\
&= -\frac{1}{\sigma^2} \mathcal{A}(\sigma, r_c) \{c_i(t)(\vec{r} - \vec{r}_i(t))\}
\end{aligned} \tag{4.14}$$

and thus for the coarse-grained density in particular

$$\begin{aligned}
\frac{\partial}{\partial \vec{r}} &= -\frac{1}{\bar{\rho}^2(\vec{r}, t)} \frac{\partial}{\partial \vec{r}} \bar{\rho}(\vec{r}, t) \\
&= \frac{1}{\bar{\rho}^2(\vec{r}, t) \sigma^2} \mathcal{A}(\sigma, r_c) \{m_i(\vec{r} - \vec{r}_i(t))\}
\end{aligned} \tag{4.15}$$

which finally leads to the expression of the linearised shear strain as function of the positions, masses and displacements of the particles, and the coarse-grained density

$$\begin{aligned}
\varepsilon_{xy}(\vec{r}, t, t + \Delta t) &= \frac{1}{2} \left[\frac{1}{\bar{\rho}^2(\vec{r}, t) \sigma^2} \left(\mathcal{A}(\sigma, r_c) \{m_i(y - y_i(t))\} \times \mathcal{A}(\sigma, r_c) \{u_x(\vec{r}_i(t), t, t + \Delta t)\} \right. \right. \\
&\quad \left. \left. + \mathcal{A}(\sigma, r_c) \{m_i(x - x_i(t))\} \times \mathcal{A}(\sigma, r_c) \{u_y(\vec{r}_i(t), t, t + \Delta t)\} \right) \right. \\
&\quad \left. - \frac{1}{\bar{\rho}(\vec{r}, t) \sigma^2} \left(\mathcal{A}(\sigma, r_c) \{u_x(\vec{r}_i(t), t, t + \Delta t)(y - y_i(t))\} \right. \right. \\
&\quad \left. \left. + \mathcal{A}(\sigma, r_c) \{u_y(\vec{r}_i(t), t, t + \Delta t)(x - x_i(t))\} \right) \right] \tag{4.16}
\end{aligned}$$

Computation details

We divide the system square box in $N_{cases} \times N_{cases}$ linearly spaced square boxes with centres $(\vec{R}_{kl})_{1 \leq k, l \leq N_{cases}}$. We then choose S_{max} times $(t_m)_{1 \leq m \leq S_{max}}$, with $\forall m, t_m \geq S_{init}$.

In our model, we consider $\forall i \in \llbracket 1; N \rrbracket, m_i = 1$.

We then have S_{max} grids of linearised shear strain $(\varepsilon_{xy,kl}(t_m, t_m + \Delta t))_{1 \leq k, l \leq N_{cases}}$, defined $\forall k, l \in \llbracket 1; N_{cases} \rrbracket$ by

$$\begin{aligned} \varepsilon_{xy,kl}(t_m, t_m + \Delta t) = & \frac{1}{2} \left[\frac{1}{\bar{\rho}^2(\vec{R}_{kl}, t_m)\sigma^2} \left(\mathcal{A}(\sigma, r_c) \{Y_{kl} - y_i(t_m)\} \times \mathcal{A}(\sigma, r_c) \{u_x(\vec{r}_i(t_m), t_m, t_m + \Delta t)\} \right. \right. \\ & + \mathcal{A}(\sigma, r_c) \{X_{kl} - x_i(t)\} \times \mathcal{A}(\sigma, r_c) \{u_y(\vec{r}_i(t_m), t_m, t_m + \Delta t)\} \Big) \\ & - \frac{1}{\bar{\rho}(\vec{R}_{kl}, t_m)\sigma^2} \left(\mathcal{A}(\sigma, r_c) \{u_x(\vec{r}_i(t), t_m, t_m + \Delta t)(Y_{kl} - y_i(t))\} \right. \\ & \left. \left. + \mathcal{A}(\sigma, r_c) \{u_y(\vec{r}_i(t), t_m, t_m + \Delta t)(X_{kl} - x_i(t))\} \right) \right] \end{aligned} \quad (4.17)$$

according to equation 4.16.

Since we have a cut-off radius r_c , we can resort to neighbour lists to speed up coarse-graining steps, *i.e.* evaluations of $\mathcal{A}(\sigma, r_c)\{\dots\}$ expressions. We have thus implemented cell lists [49].

We can now take the Fourier transforms of the linearised shear strain grids of equation 4.17

$$(\tilde{\varepsilon}_{xy,kl}(t_m, t_m + \Delta t))_{1 \leq k, l \leq N_{cases}} = \mathcal{F} \{ (\varepsilon_{xy,pq}(t_m, t_m + \Delta t))_{1 \leq p, q \leq N_{cases}} \} (\vec{K}_{kl}, t_m, t_m + \Delta t) \quad (4.18)$$

with $(\vec{K}_{kl})_{1 \leq k, l \leq N_{cases}}$ the grid of wave vectors, then compute the linearised shear strain correlation grid

$$C_{\varepsilon_{xy}\varepsilon_{xy}}(\vec{R}_{kl}, \Delta t) = \frac{\mathcal{F}^{-1} \left\{ \left(\sum_m |\tilde{\varepsilon}_{xy,pq}(t_m, t_m + \Delta t)|^2 \right)_{1 \leq p, q \leq N_{cases}} \right\} (\vec{R}_{kl})}{\sum_m \sum_{p,q} \tilde{\varepsilon}_{xy,pq}^2(t_m, t_m + \Delta t)} \quad (4.19)$$

Our computation script is available at [github.com/yketa/active_particles/analysis/css.py](#).

4.3.2 Results

High activity ($\text{Pe} > \text{Pe}_t$)

We investigate shear strain correlations in a system in phase separated state at high activity.

We observe in the shear strain map of figure 4.1 that the highest values of shear strain in absolute value are found at the interface between the dense fluid and the active gas. This finding is not surprising since we are dealing here with an interface between phases of very different motilities.

We then observe in the shear strain correlation map of figure 4.1 that $C_{\varepsilon_{xy}\varepsilon_{xy}}(\Delta \vec{r}, \Delta t)$ effectively has a quadropolar symmetry as observed in the litterature [44, 45]. This confirms the relevance of the introduction of the $C_4^4(\Delta r, \Delta t)$ function (see equation 4.5).

We have graphically checked that there existed a region of the system where an active gas hole never opened and found that it was the case for a square region of centre $(x = -150, y = 150)$ and length $L = 300$. We have then looked at strain correlations restricted to this area only. We show in figure 4.2 the resulting strain correlation map. By comparison with figure 4.1, we find that the strain correlation map is sharper if active gas holes are removed.

We however stress that this kind of manipulation is not possible for all our systems in the phase separated regime. Indeed, just above the transition from fluid states to phase separated states, multiple smaller and transient active gas holes appear in the system. These holes get bigger as the activity increases until, as in

the system we are currently studying, a single hole appears, which size and position hardly vary during the simulation time. This observation has also already been made for other active systems [3, 16].

$$N = 1.00e + 05, \phi = 0.80, \tilde{v} = 1.00e - 02, \tilde{\nu}_r = 2.00e - 05, \bar{N} = 1.00e + 05, \Delta t = 1.00e + 03, nD_0\Delta t = 6.28e + 02 \\ L = 6.31e + 02, x_0 = 0.00e + 00, y_0 = 0.00e + 00, S_{init} = 5.00e + 03, S_{max} = 1.00e + 00, N_{cases} = 5.00e + 02, r_{cut} = 2.00e + 00, \sigma = 2.00e + 00$$

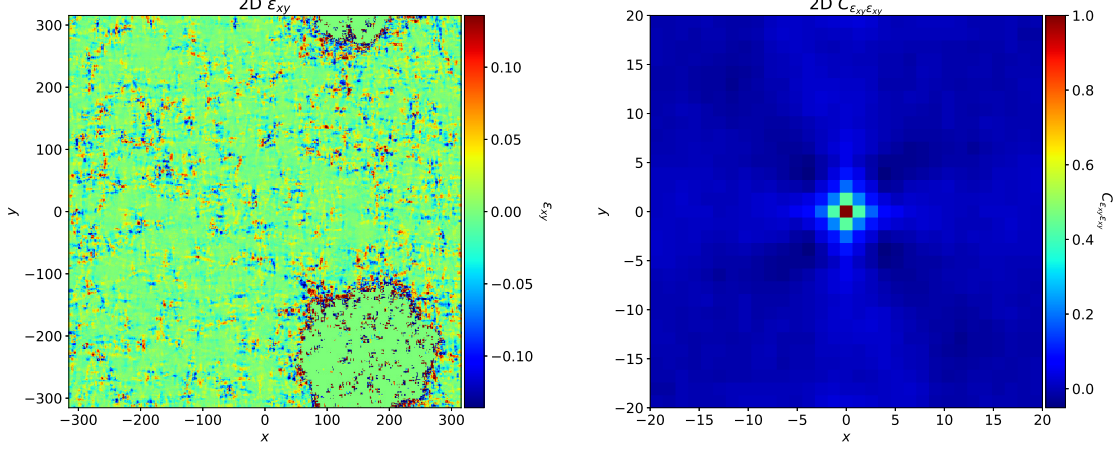


Figure 4.1: Shear strain correlations, calculated with the real space method (see section 4.3.1), at packing fraction $\phi = 0.80$, self-propelling velocity $\tilde{v} = 1 \cdot 10^{-2}$, and rotational diffusion rate $\tilde{\nu}_r = 2 \cdot 10^{-5}$ (phase separated regime). We have the average particle separation $a \approx 2$. **(left)** Shear strain map, $\varepsilon_{xy}(\vec{r} \equiv (x, y), t, t + \Delta t)$. There is an open active gas hole in the system, visible on the top and bottom right corners. **(right)** Shear strain correlation map, $C_{\varepsilon_{xy}\varepsilon_{xy}}(\Delta\vec{r} \equiv (x, y), \Delta t)$.

$$N = 1.00e + 05, \phi = 0.80, \tilde{v} = 1.00e - 02, \tilde{\nu}_r = 2.00e - 05 \\ S_{init} = 5.00e + 02, \Delta t = 1.00e + 00, S_{max} = 1.00e + 02, N_{cases} = 1.00e + 03, r_{cut} = 2.00e + 00, \sigma = 2.00e + 00$$

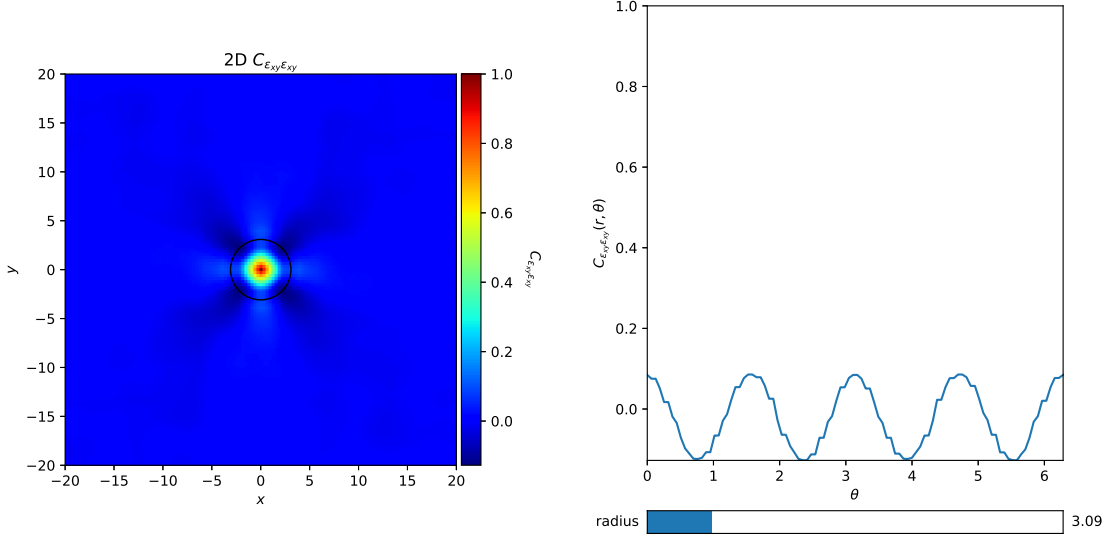


Figure 4.2: Shear strain correlations, calculated with the real space method (see section 4.3.1), at packing fraction $\phi = 0.80$, self-propelling velocity $\tilde{v} = 1 \cdot 10^{-2}$, and rotational diffusion rate $\tilde{\nu}_r = 2 \cdot 10^{-5}$ (phase separated regime), from the square box of centre $(x = -150, y = 150)$ and length $L = 300$ in the system of figure 4.1. We have the average particle separation $a \approx 2$. **(left)** Shear strain correlation map, $C_{\varepsilon_{xy}\varepsilon_{xy}}(\Delta\vec{r} \equiv (x, y), \Delta t)$. The black circle materialises the radial projection of the shear strain correlation. **(right)** Radial projection of the shear strain correlation on a circle of radius $r = 3.09$, $C_{\varepsilon_{xy}\varepsilon_{xy}}(r = 3.09, \theta), \Delta t$.

We calculated shear strain correlations $C_{\varepsilon_{xy}\varepsilon_{xy}}(\Delta\vec{r}, \Delta t)$ for the subsystem of figure 4.2 at different lag times Δt , then projected them on $\cos 4\theta$ according to equation 4.5 to obtain $C_4^4(\Delta r, \Delta t)$. These are shown in figure 4.3.

Our curves are quite similar to the equivalent ones reported in [44, 45]. We have a peak of $C_4^4(\Delta r, \Delta t)$ close to 2 units of average particle separation and curves collapse, at least for $nD_0\Delta t \lesssim 30$. Our most relevant observation is that our curves are quite consistent with an algebraic decay $(r/a)^{-2}$, indicating scale free correlations reminiscent of a glass-forming material at low temperature, as discussed in section 4.1.

We however have smooth but large fluctuations around this fit, which origin is still unknown.

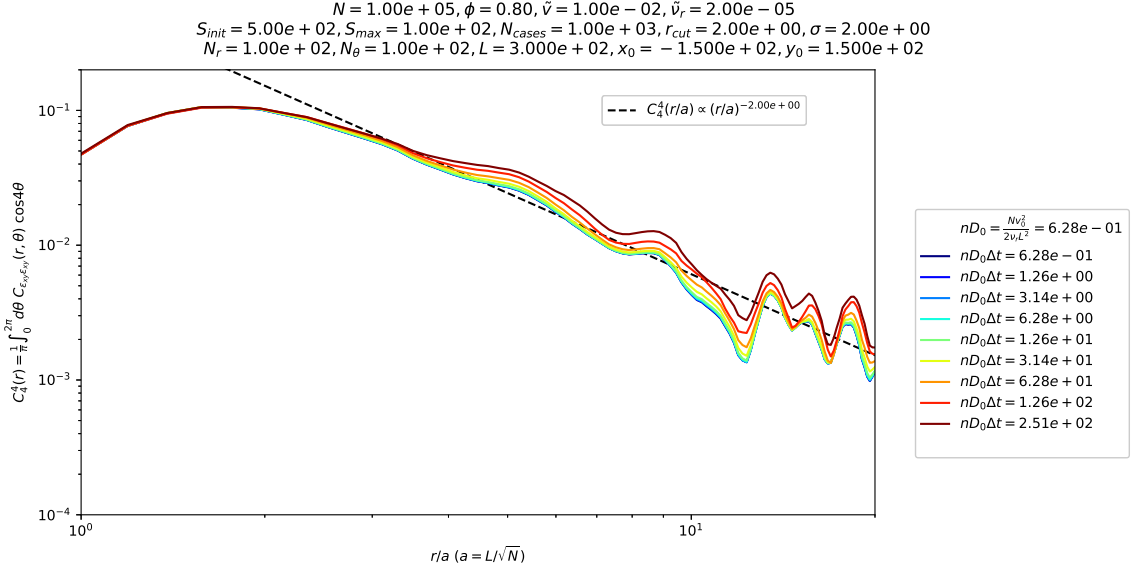


Figure 4.3: Projection of shear strain correlations on $\cos 4\theta$, $C_4^4(\Delta r, \Delta t)$, according to equation 4.5, at packing fraction $\phi = 0.80$, self-propelling velocity $\tilde{v} = 1 \cdot 10^{-2}$, and rotational diffusion rate $\tilde{\nu}_r = 2 \cdot 10^{-5}$ (phase separated regime), for a subsystem containing no active gas holes, for different lag times Δt . We have $n = N/L^2$ the number density of particles and $D_0 = V_0^2/2\nu_r$ the diffusion constant of a single particle, introduced for matter of comparison of lag times between different systems as suggested in [44]. The dashed line corresponds to an arbitrary fit to a power law $(r/a)^{-2}$.

Low activity ($\text{Pe} < \text{Pe}_t$)

We calculated shear strain correlations $C_{\varepsilon_{xy}\varepsilon_{xy}}(\Delta\vec{r}, \Delta t)$ for a system in fluid state, at different lag times Δt , then projected them on $\cos 4\theta$ according to equation 4.5 to obtain $C_4^4(\Delta r, \Delta t)$. These are shown in figure 4.4.

We still observe a peak of $C_4^4(\Delta r, \Delta t)$ close to 2 units of average particle separation, however, contrarily to the phase separated state (see figure 4.3), we observe here an exponential decay of the shear strain correlation, which length scale is approximately equal to 2 units of average particle separation. A simple exponential decay of correlations is indeed what we would expect in a liquid above the melting point [50]. We finally add that the length scale of this decay increases sensitively with increasing lag time Δt .

There must then be a transition from an exponential to an algebraic decay of shear strain correlations as activity increases which we need to characterise.

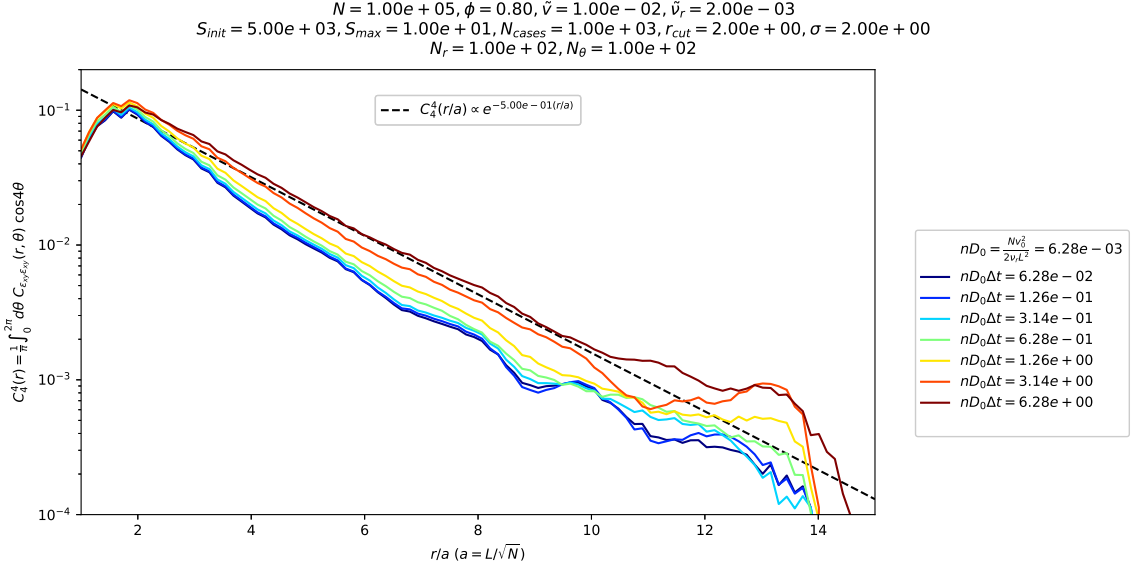


Figure 4.4: Projection of shear strain correlations on $\cos 4\theta$, $C_4^4(\Delta r, \Delta t)$, according to equation 4.5, at packing fraction $\phi = 0.80$, self-propelling velocity $\tilde{v} = 1 \cdot 10^{-2}$, and rotational diffusion rate $\tilde{\nu}_r = 2 \cdot 10^{-3}$ (fluid regime), for different lag times Δt . We have $n = N/L^2$ the number density of particles and $D_0 = V_0^2/2\nu_r$ the diffusion constant of a single particle, introduced for matter of comparison of lag times between different systems as suggested in [44]. The dashed line corresponds to an arbitrary fit to an exponential $\exp(-r/2a)$.

Issue

Despite this method giving interesting and encouraging results, we deplore its exceptional slowness despite our best computational efforts. We introduce in section 4.4 new quantities enabling us to compute shear strain correlations more quickly and efficiently.

4.4 Collective mean square displacement method

4.4.1 Collective mean square displacement

Definition

We take the Fourier transform of the displacement of the particle at position \vec{r} at time t between times t and $t + \Delta t$, evaluated at wave vector \vec{k} such that $k = ||\vec{k}|| \neq 0$

$$\tilde{\vec{u}}(\vec{k}, t, t + \Delta t) = \mathcal{F}\{\vec{u}(\vec{r}, t, t + \Delta t)\}(\vec{k}) \quad (4.20)$$

and introduce

$$\begin{aligned} \vec{e}_{||} &= \vec{k}/k && \parallel \vec{k} \\ \vec{e}_{\perp} &= (\vec{e}_z \wedge \vec{k})/k && \perp \vec{k} \end{aligned} \quad (4.21)$$

with $\phi = (\vec{e}_x; \vec{e}_{||})$, such that we can decompose $\tilde{\vec{u}}(\vec{k}, t, t + \Delta t)$ in this base [51]

$$\begin{aligned} \begin{pmatrix} \tilde{u}_x(\vec{k}, t, t + \Delta t) \\ \tilde{u}_y(\vec{k}, t, t + \Delta t) \end{pmatrix} &= \begin{pmatrix} \cos \phi & -\sin \phi \\ \sin \phi & \cos \phi \end{pmatrix} \begin{pmatrix} \tilde{u}_{||}(\vec{k}, t, t + \Delta t) \\ \tilde{u}_{\perp}(\vec{k}, t, t + \Delta t) \end{pmatrix} \\ &= \begin{pmatrix} k_x/k & -k_y/k \\ k_y/k & k_x/k \end{pmatrix} \begin{pmatrix} \tilde{u}_{||}(\vec{k}, t, t + \Delta t) \\ \tilde{u}_{\perp}(\vec{k}, t, t + \Delta t) \end{pmatrix} \end{aligned} \quad (4.22)$$

With these notations, we introduce the longitudinal and transversal mean square displacements [44, 52], respectively $C^{\parallel}(k, \Delta t)$ and $C^{\perp}(k, \Delta t)$, defined by

$$\begin{aligned} C^{\parallel}(k, \Delta t) &= \left\langle |\tilde{u}_{\parallel}(\vec{k}, t, t + \Delta t)|^2 \right\rangle \\ C^{\perp}(k, \Delta t) &= \left\langle |\tilde{u}_{\perp}(\vec{k}, t, t + \Delta t)|^2 \right\rangle \end{aligned} \quad (4.23)$$

where $\langle \dots \rangle$ denotes an average over time t and directions of \vec{k} at fixed norm k . These functions are collective and spatially resolved generalisations of the mean square displacement [44].

We note in [44] that for an incompressible glass

$$\begin{aligned} C^{\parallel}(k, \Delta t) &= 0 \\ C^{\perp}(k, \Delta t) &\underset{\frac{2\pi}{k} \gg a}{\propto} k^{-2} \end{aligned} \quad (4.24)$$

with a the average interparticle distance. Authors of [53] also report

$$\begin{aligned} C^{\parallel}(k, \Delta t) &\underset{\frac{2\pi}{k} \gg a}{\propto} k^{-2} \\ C^{\perp}(k, \Delta t) &\underset{\frac{2\pi}{k} \gg a}{\propto} k^{-2} \end{aligned} \quad (4.25)$$

in a polydisperse Lennard-Jones mixture under shear.

Shear strain correlation

We have from [44] a simple relation between shear strain correlations and collective mean square displacements

$$C_{\varepsilon_{xy}\varepsilon_{xy}}(\Delta \vec{r}, \Delta t) = \mathcal{F}^{-1} \left\{ -\frac{k_x^2 k_y^2}{k^2} \left(C^{\perp}(k, \Delta t) - C^{\parallel}(k, \Delta t) \right) + \frac{k^2}{4} C^{\perp}(k, \Delta t) \right\} (\Delta \vec{r}) \quad (4.26)$$

hence our interest in these functions.

This relation can be derived from

$$C_{\varepsilon_{xy}\varepsilon_{xy}}(\Delta \vec{r}, \Delta t) = \mathcal{F}^{-1} \left\{ \left\langle \left| \mathcal{F} \{ \varepsilon_{xy}(\vec{r}, t, t + \Delta t) \} (\vec{k}) \right|^2 \right\rangle_t \right\} (\Delta \vec{r}) \quad (4.27)$$

according to appendix A.1, in which we can replace $u_x(\vec{r}, t, t + \Delta t)$ and $u_y(\vec{r}, t, t + \Delta t)$ by their expressions in terms of $\tilde{u}_{\parallel}(\vec{k}, t, t + \Delta t)$ and $\tilde{u}_{\perp}(\vec{k}, t, t + \Delta t)$ with equation 4.22, leading to equation 4.26 [51].

Computation details

First of all, we can note that

$$\begin{aligned} C^{\parallel}(k, \Delta t) &= \frac{1}{k^2} \left\langle |\vec{k} \cdot \tilde{u}(\vec{k}, t, t + \Delta t)|^2 \right\rangle \\ C^{\perp}(k, \Delta t) &= \frac{1}{k^2} \left\langle ||\vec{k} \wedge \tilde{u}(\vec{k}, t, t + \Delta t)||^2 \right\rangle \end{aligned} \quad (4.28)$$

which expression are used in [53].

We divide the system square box in $N_{cases} \times N_{cases}$ linearly spaced square boxes with centres $(\vec{R}_{kl})_{1 \leq k, l \leq N_{cases}}$. With dL the length of each box, we introduce

$$\vec{u}_{kl}(t, t + \Delta t) = \text{mean} \left(\left\{ \vec{u}(\vec{r}_i(t), t, t + \Delta t), \|\vec{r}_i(t) - \vec{R}_{kl}\|_{+\infty} \leq \frac{dL}{2} \right\} \right) \quad (4.29)$$

the average displacement of particles in each box between times t and $t + \Delta t$. We then choose S_{max} times $(t_m)_{1 \leq m \leq S_{max}}$, with $\forall m, t_m \geq S_{init}$.

We now have $\forall m$, a displacement grid $(\vec{u}_{kl}(t_m, t_m + \Delta t))_{1 \leq k, l \leq N_{cases}}$ of which we can take the Fast Fourier Transform

$$(\tilde{\vec{u}}_{kl}(t_m, t_m + \Delta t))_{1 \leq k, l \leq N_{cases}} = \mathcal{F} \{ (\vec{u}_{pq}(t_m, t_m + \Delta t))_{1 \leq p, q \leq N_{cases}} \} (\vec{K}_{kl}, t_m, t_m + \Delta t) \quad (4.30)$$

with $(\vec{K}_{kl})_{1 \leq k, l \leq N_{cases}}$ the grid of wave vectors, then compute the collective mean square displacements

$$\begin{aligned} C^\perp(\vec{K}_{kl}, \Delta t) &= \frac{1}{S_{max} \|\vec{K}_{kl}\|^2} \sum_m \|\vec{K}_{kl} \wedge \tilde{\vec{u}}_{kl}(t_m, t_m + \Delta t)\|^2 \\ C^{\parallel}(\vec{K}_{kl}, \Delta t) &= \frac{1}{S_{max} \|\vec{K}_{kl}\|^2} \sum_m |\vec{K}_{kl} \cdot \tilde{\vec{u}}_{kl}(t_m, t_m + \Delta t)|^2 \end{aligned} \quad (4.31)$$

according to equation 4.28. Please note that these functions are slightly different than the one introduced in equation 4.23 since they now depend on the wave vector rather than its sole norm. We have verified that either definitions gave consistent results and kept this version for algorithmic simplicity.

We can then compute the Fourier transform of the shear strain correlation

$$F_{kl}(\Delta t) = -\frac{K_{kl,x}^2 K_{kl,y}^2}{K_{kl}^2} (C^\perp(\vec{K}_{kl}, \Delta t) - C^{\parallel}(\vec{K}_{kl}, \Delta t)) + \frac{K_{kl}^2}{4} C^\perp(\vec{K}_{kl}, \Delta t) \quad (4.32)$$

according to equation 4.26, and finally obtain the shear strain correlation through inverse Fast Fourier Transform

$$C_{\varepsilon_{xy} \varepsilon_{xy}}(\vec{R}_{kl}, \Delta t) = \frac{\mathcal{F}^{-1} \left\{ (F_{pq}(\Delta t))_{1 \leq p, q \leq N_{cases}} \right\}(\vec{R}_{kl})}{\mathcal{F}^{-1} \left\{ (F_{pq}(\Delta t))_{1 \leq p, q \leq N_{cases}} \right\}(\vec{0})} \quad (4.33)$$

Our computation script is available at [github/yketa/active_particles/analysis/ctt.py](#).

4.4.2 Results

Preliminary results

First of all, we point out that computing collective mean square displacements is orders of magnitude quicker than computing coarse-grained displacements as described in section 4.3.1. This method then seems better suited to systematically analyse shear strain correlations within our model.

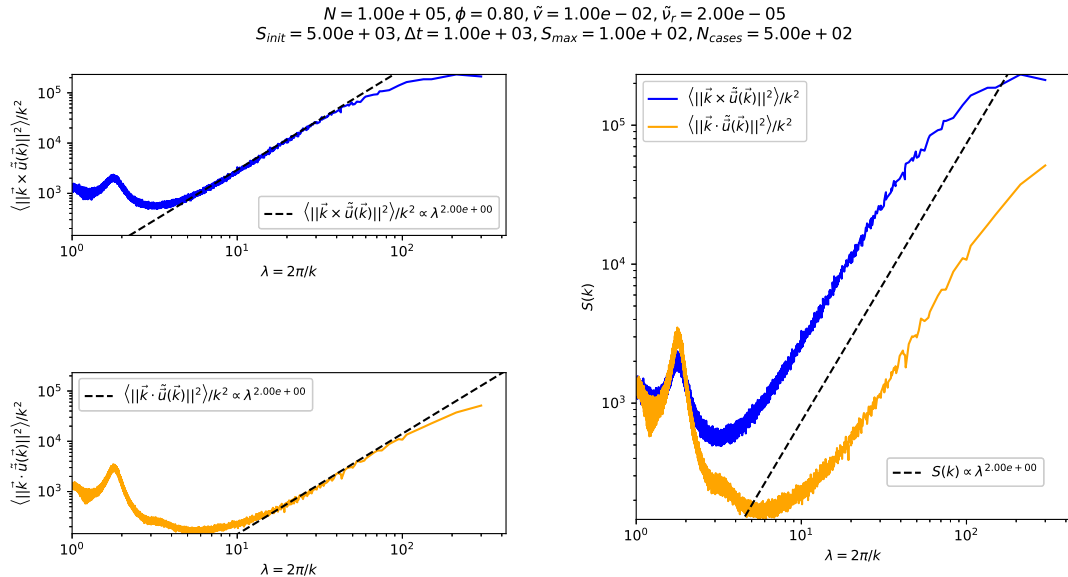


Figure 4.5: Collective mean square displacements according to equation 4.23, at packing fraction $\phi = 0.80$, self-propelling velocity $\tilde{v} = 1 \cdot 10^{-2}$, and rotational diffusion rate $\tilde{\nu}_r = 2 \cdot 10^{-5}$ (phase separated regime). Dashed lines correspond to arbitrary fits to a power law λ^2 . **(top left)** Transversal collective mean square displacement $C^\perp(k, \Delta t) = \langle \|\vec{k} \wedge \tilde{\vec{u}}(\vec{k}, t, t + \Delta t)\|^2 \rangle$ as function of the wavelength $\lambda = 2\pi/k$. **(bottom left)** Longitudinal collective mean square displacement $C^{\parallel}(k, \Delta t) = \langle \|\vec{k} \cdot \tilde{\vec{u}}(\vec{k}, t, t + \Delta t)\|^2 \rangle$ as function of the wavelength $\lambda = 2\pi/k$. **(right)** Superimposition of the transversal (blue) and longitudinal (orange) collective mean square displacements.

We first calculated collective mean square displacements in a system in the phase separated state. This calculation has been performed on the whole system, *i.e.* including the active gas phase. We present our results in figure 4.5.

We observe in figure 4.5 that the longitudinal collective mean square displacement $C^{\parallel}(k, \Delta t)$ is a strictly positive function, indicating that our system is compressible [44] which was an expected finding. We however note that the longitudinal part $C^{\parallel}(k, \Delta t)$ is about an order of magnitude lesser than the transversal part $C^{\perp}(k, \Delta t)$ of the collective mean square displacement, as reported in [53].

Both $C^{\parallel}(k, \Delta t)$ and $C^{\perp}(k, \Delta t)$ are quite well fitted with a power law k^{-2} for about a decade ($10 \lesssim \lambda = 2\pi/k \lesssim 20$), which was also reported in [53] and may indicate elastic properties of the system. This algebraic behaviour is limited at high wavelengths by finite-size effects and at low wavelengths by the discrete microscopic structure of the system. Indeed, we have that the peak in both $C^{\parallel}(k, \Delta t)$ and $C^{\perp}(k, \Delta t)$ at $\lambda = 2\pi/k \approx a \approx 2$ with a the average particle separation is a consequence of the discreteness of the displacement field.

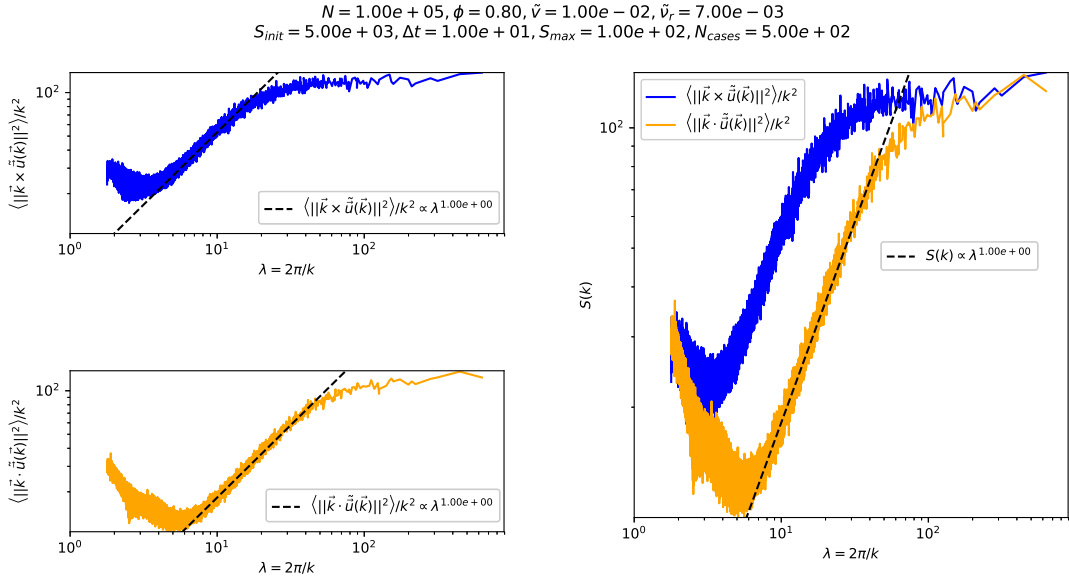


Figure 4.6: Collective mean square displacements according to equation 4.23, at packing fraction $\phi = 0.80$, self-propelling velocity $\tilde{v} = 1 \cdot 10^{-2}$, and rotational diffusion rate $\tilde{\nu}_r = 7 \cdot 10^{-3}$ (fluid regime). Dashed lines correspond to arbitrary fits to a power law λ . **(top left)** Transversal collective mean square displacement $C^{\perp}(k, \Delta t) = \left\langle \|\vec{k} \wedge \tilde{u}(\vec{k}, t, t + \Delta t)\|^2 \right\rangle$ as function of the wavelength $\lambda = 2\pi/k$. **(bottom left)** Longitudinal collective mean square displacement $C^{\parallel}(k, \Delta t) = \left\langle \|\vec{k} \cdot \tilde{u}(\vec{k}, t, t + \Delta t)\|^2 \right\rangle$ as function of the wavelength $\lambda = 2\pi/k$. **(right)** Superimposition of the transversal (blue) and longitudinal (orange) collective mean square displacements.

We then calculated collective mean square displacements in a system in the fluid state. We present our results in figure 4.6.

As in the high activity case (see figure 4.5), we observe that the longitudinal collective mean square displacement $C^{\parallel}(k, \Delta t)$ is a strictly positive function. Nonetheless, we notice in this low activity case that the values of $C^{\parallel}(k, \Delta t)$ and $C^{\perp}(k, \Delta t)$ are of the same order of magnitude.

Both $C^{\parallel}(k, \Delta t)$ and $C^{\perp}(k, \Delta t)$ are quite well fitted with a power law k^{-1} for about a decade ($6 \lesssim \lambda = 2\pi/k \lesssim 60$). However, this exponent for the power law decay of the collective mean square displacements with increasing wave vector norm is puzzling and further investigations are needed to understand it.

Necessity of filtering

We use the collective mean square displacements presented in figure 4.5 to compute shear strain correlations $C_{\varepsilon_{xy}\varepsilon_{xy}}(\Delta\vec{r}, \Delta t)$ according to equation 4.26. Our results are presented in figure 4.7.

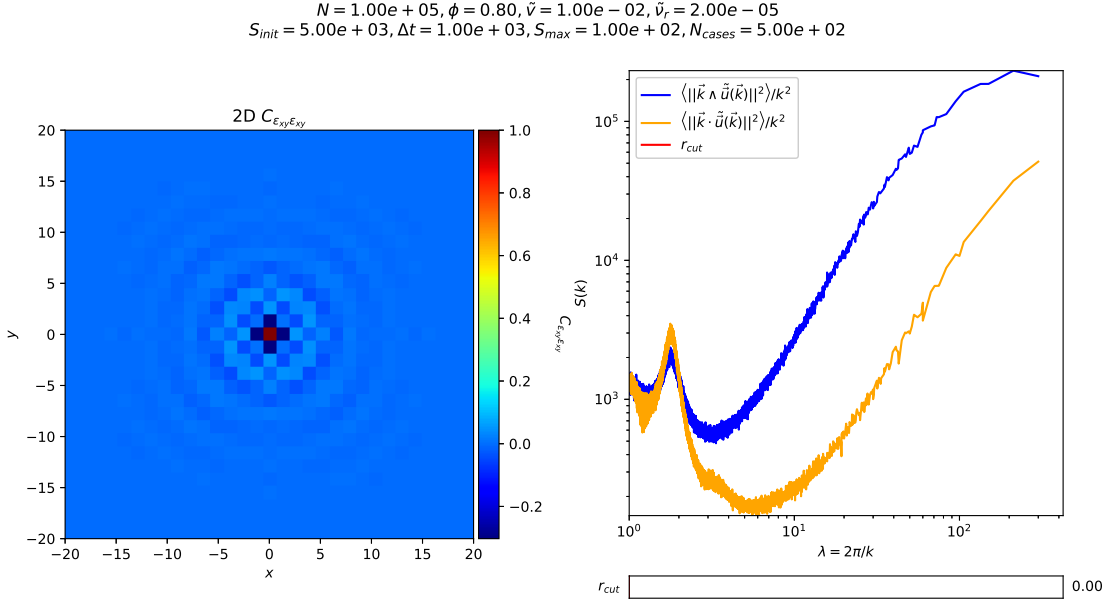


Figure 4.7

We have that shear strain correlations are completely drowned under a pattern of concentric waves which spatial period is close to the average particle separation $a \approx 2$. As we had discussed on figure 3.2, these waves originate from the fact that our gridding is so tight that we are resolving the microscopic structure of the system. This is visible in the collective mean displacement curves (figures 4.5 and 4.6) in the form of a peak near $\lambda = a$.

As a solution to this inconvenience, we propose to filter out low wavelengths corresponding to the microscopic structure. This is a form of coarse-graining since it means to eliminate short range degrees of freedom. A first attempt has been to set all Fourier components under a given wavelength to 0, yet this was doomed to failure since completely depriving a signal of its high frequency components is a cause of ringing artifacts [54]. A better solution is to perform, as we have done for displacements in the real space method (see section 4.3.1), a Gaussian coarse-graining of the shear strain.

We introduce the Gaussian filtering function

$$\mathcal{G}(\vec{r}, r_c) = \frac{1}{2\pi\sigma^2} \exp\left(-\frac{||\vec{r}||^2}{2\sigma^2}\right) \quad (4.34)$$

where r_c is the spatial extent of the function, such that the coarse-grained version of the shear strain, $\varepsilon_{xy}^{(cg)}(\vec{r}, t, t + \Delta t)$, is obtained by convolution

$$\varepsilon_{xy}^{(cg)}(\vec{r}, t, t + \Delta t) = \int_{\mathbb{R}^2} d^2\vec{r}' \mathcal{G}(\vec{r}' - \vec{r}, r_c) \varepsilon_{xy}^{(cg)}(\vec{r}', t, t + \Delta t) = [\mathcal{G} * \varepsilon_{xy}](\vec{r}, t, t + \Delta t) \quad (4.35)$$

We thus obtain in equation 4.27, when deriving shear strain correlations from coarse-grained shear strain

$$\begin{aligned} C_{\varepsilon_{xy}\varepsilon_{xy}}(\Delta\vec{r}, \Delta t) &= \mathcal{F}^{-1} \left\{ \left\langle \left| \mathcal{F} \left\{ \varepsilon_{xy}^{(cg)}(\vec{r}, t, t + \Delta t) \right\} (\vec{k}) \right|^2 \right\rangle_t \right\} (\Delta\vec{r}) \\ &= \mathcal{F}^{-1} \left\{ \left\langle \left| \mathcal{F} \{ [\mathcal{G} * \varepsilon_{xy}](\vec{r}, t, t + \Delta t) \} (\vec{k}) \right|^2 \right\rangle_t \right\} (\Delta\vec{r}) \\ &= \mathcal{F}^{-1} \left\{ \left\langle \left| \mathcal{F} \{ \varepsilon_{xy}(\vec{r}, t, t + \Delta t) \} (\vec{k}) \right|^2 \right\rangle_t \tilde{\mathcal{G}}(\vec{k}, r_c)^2 \right\} (\Delta\vec{r}) \end{aligned} \quad (4.36)$$

where we have used the convolution theorem, and with $\tilde{\mathcal{G}}(\vec{k}, r_c)$ the Fourier transform of the Gaussian filtering function

$$\tilde{\mathcal{G}}(\vec{k}, r_c) = \frac{1}{2\pi\sigma^2} \int_{\mathbb{R}^2} d^2\vec{r} e^{-i\vec{k}\cdot\vec{r}} \exp\left(-\frac{||\vec{r}||^2}{2r_c^2}\right) = \exp\left(-\frac{1}{2}r_c^2||\vec{k}||^2\right) \quad (4.37)$$

Coarse-graining is then performed by multiplying the shear strain correlation Fourier transform in equation 4.32 with the square of the Gaussian filtering function Fourier transform in equation 4.37.

Results with Gaussian filter

We use the collective mean square displacements presented in figure 4.5 to compute shear strain correlations $C_{\varepsilon_{xy}\varepsilon_{xy}}(\Delta\vec{r}, \Delta t)$ according to equation 4.26, this time using a Gaussian filter. Our results are presented in figure 4.8.

For this system in phase separated state, we recover the results of figure 4.3, *i.e.* we have a peak of $C_4^4(\Delta r, \Delta t)$ close to 2 units of average particle separation and curves collapse, at least for $nD_0\Delta t \lesssim 130$. Moreover, our curves are quite consistent with an algebraic decay $(r/a)^{-2}$, indicating scale free correlations reminiscent of a glass-forming material at low temperature.

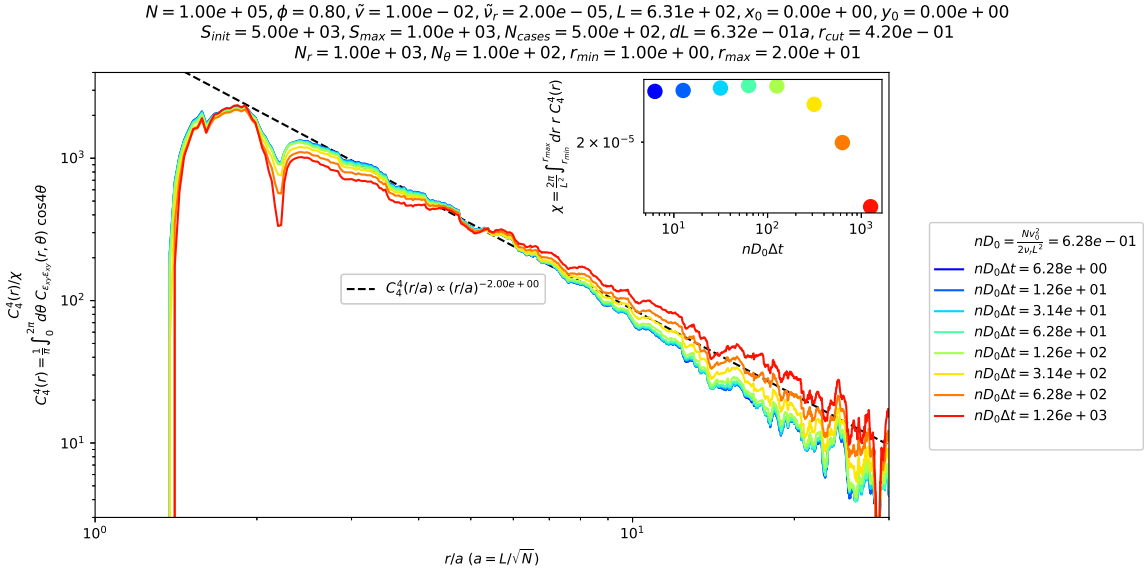


Figure 4.8: Projection of shear strain correlations on $\cos 4\theta$, $C_4^4(\Delta r, \Delta t)$ according to equation 4.5, normalised by its susceptibility $\chi = \int dr 2\pi r C_4^4(r, \Delta t)$, at packing fraction $\phi = 0.80$, self-propelling velocity $\tilde{v} = 1 \cdot 10^{-2}$, and rotational diffusion rate $\tilde{\nu}_r = 2 \cdot 10^{-5}$ (phase separated regime), for different lag times Δt . A linear interpolation between grid boxes has been performed in the step from the shear strain correlation grid to the $C_4^4(\Delta r, \Delta t)$ function to smooth the curve. We have $n = N/L^2$ the number density of particles and $D_0 = V_0^2/2\nu_r$ the diffusion constant of a single particle, introduced for matter of comparison of lag times between different systems as suggested in [44]. The dashed line corresponds to an arbitrary fit to a power law $(r/a)^{-2}$.

We perform the same calculations for a system of lower activity, in the fluid regime. Our results are presented in figure 4.9.

For this system in fluid state, we recover the results of figure 4.4, *i.e.* we have a peak of $C_4^4(\Delta r, \Delta t)$ close to 2 units of average particle separation and curves collapse. Moreover, we observe an exponential decay of the correlations, with a length scale of a few particles and which is an increasing function of increasing lag time Δt .

$N = 1.00e + 05$, $\phi = 0.80$, $\tilde{v} = 1.00e - 02$, $\tilde{v}_r = 2.00e - 03$, $L = 6.31e + 02$, $x_0 = 0.00e + 00$, $y_0 = 0.00e + 00$
 $S_{init} = 5.00e + 03$, $S_{max} = 5.00e + 02$, $N_{cases} = 5.00e + 02$, $dL = 6.32e - 01a$, $r_{cut} = 4.20e - 01$
 $N_r = 1.00e + 03$, $N_\theta = 1.00e + 02$, $r_{min} = 1.00e + 00$, $r_{max} = 2.00e + 01$

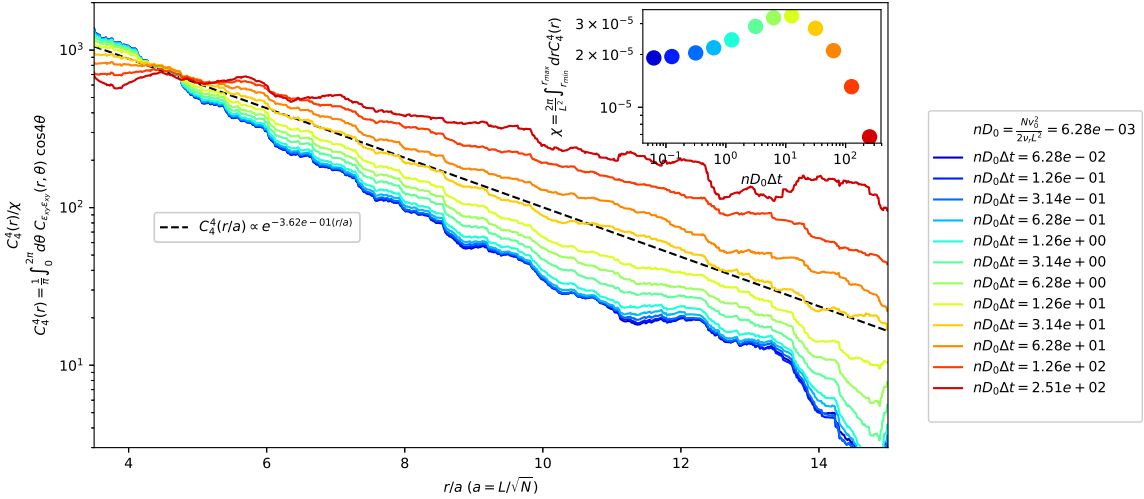


Figure 4.9: Projection of shear strain correlations on $\cos 4\theta$, $C_4^4(\Delta r, \Delta t)$ according to equation 4.5, normalised by its susceptibility $\chi = \int dr 2\pi r C_4^4(r, \Delta t)$, at packing fraction $\phi = 0.80$, self-propelling velocity $\tilde{v} = 1 \cdot 10^{-2}$, and rotational diffusion rate $\tilde{v}_r = 2 \cdot 10^{-3}$ (fluid regime), for different lag times Δt . A linear interpolation between grid boxes has been performed in the step from the shear strain correlation grid to the $C_4^4(\Delta r, \Delta t)$ function to smooth the curve. We have $n = N/L^2$ the number density of particles and $D_0 = V_0^2/2\nu_r$ the diffusion constant of a single particle, introduced for matter of comparison of lag times between different systems as suggested in [44]. The dashed line corresponds to an arbitrary fit to an exponential $\exp(-0.362(r/a))$.

We then conclude here as we have concluded in section 4.3.2: more analyses are needed to characterise the transition from exponential to algebraic decay of the shear strain correlations with increasing activity.

Conclusion

We have numerically studied a minimal model of active Brownian disks, which perform independent persistent random walks, with purely repulsive interparticle potential.

This model system displays motility-induced phase separation, a common feature of systems of self-propelled particles. We have showed that, when increasing the persistence time of the random walk of each particle, this phenomenon, in which the system spontaneously separates into a dense fluid phase of lesser motility and an active gas phase of greater motility, is accompanied by an increase of dynamic heterogeneity as measured by the cooperativity of displacements field and a decrease in the directionality of the displacement correlations. Nonetheless, such observations could not be made when increasing the activity to the point of phase separation by simply increasing the velocities of the particles. We suggest to investigate other paths through the phase diagram to rigorously establish the relevance of each parameter in this transition.

We have also brought evidence that, as the activity increases, our model system develops scale-free shear strain correlations, a common feature of glass-forming material. Our current efforts are dedicated to characterising the transition from the fluid regime to the phase separated regime as seen by the decay of these shear strain correlations.

References

- [1] Michael E Cates and Julien Tailleur. Motility-induced phase separation. *Annu. Rev. Condens. Matter Phys.*, 6(1):219–244, 2015.
- [2] M Cristina Marchetti, Jean-François Joanny, Sriram Ramaswamy, Tanniemola B Liverpool, Jacques Prost, Madan Rao, and R Aditi Simha. Hydrodynamics of soft active matter. *Reviews of Modern Physics*, 85(3):1143, 2013.
- [3] Demian Levis and Ludovic Berthier. Clustering and heterogeneous dynamics in a kinetic monte carlo model of self-propelled hard disks. *Physical Review E*, 89(6):062301, 2014.
- [4] Christopher Dombrowski, Luis Cisneros, Sunita Chatkaew, Raymond E Goldstein, and John O Kessler. Self-concentration and large-scale coherence in bacterial dynamics. *Physical review letters*, 93(9):098103, 2004.
- [5] Thomas E Angelini, Edouard Hannezo, Xavier Trepat, Manuel Marquez, Jeffrey J Fredberg, and David A Weitz. Glass-like dynamics of collective cell migration. *Proceedings of the National Academy of Sciences*, 108(12):4714–4719, 2011.
- [6] Daniel S Calovi, Ugo Lopez, Sandrine Ngo, Clément Sire, Hugues Chaté, and Guy Theraulaz. Swarming, schooling, milling: phase diagram of a data-driven fish school model. *New journal of Physics*, 16(1):015026, 2014.
- [7] Andrea Cavagna and Irene Giardina. Bird flocks as condensed matter. *Annu. Rev. Condens. Matter Phys.*, 5(1):183–207, 2014.
- [8] Gabriel Popkin. The physics of life. *Nature News*, 529(7584):16, 2016.
- [9] Hisashi Haga, Chikako Irahara, Ryo Kobayashi, Toshiyuki Nakagaki, and Kazushige Kawabata. Collective movement of epithelial cells on a collagen gel substrate. *Biophysical journal*, 88(3):2250–2256, 2005.
- [10] Peter Friedl and Darren Gilmour. Collective cell migration in morphogenesis, regeneration and cancer. *Nature reviews Molecular cell biology*, 10(7):445, 2009.
- [11] Simon Garcia, Edouard Hannezo, Jens Elgeti, Jean-François Joanny, Pascal Silberzan, and Nir S Gov. Physics of active jamming during collective cellular motion in a monolayer. *Proceedings of the National Academy of Sciences*, 112(50):15314–15319, 2015.
- [12] Tamás Vicsek, András Czirók, Eshel Ben-Jacob, Inon Cohen, and Ofer Shochet. Novel type of phase transition in a system of self-driven particles. *Physical review letters*, 75(6):1226, 1995.
- [13] Balint Szabo, GJ Szöllösi, B Gönci, Zs Jurányi, David Selmeczi, and Tamás Vicsek. Phase transition in the collective migration of tissue cells: experiment and model. *Physical Review E*, 74(6):061908, 2006.
- [14] Jonathan R Howse, Richard AL Jones, Anthony J Ryan, Tim Gough, Reza Vafabakhsh, and Ramin Golestanian. Self-motile colloidal particles: from directed propulsion to random walk. *Physical review letters*, 99(4):048102, 2007.
- [15] I Theurkauff, C Cottin-Bizonne, J Palacci, C Ybert, and L Bocquet. Dynamic clustering in active colloidal suspensions with chemical signaling. *Physical review letters*, 108(26):268303, 2012.
- [16] Adam Wysocki, Roland G Winkler, and Gerhard Gompper. Cooperative motion of active brownian spheres in three-dimensional dense suspensions. *EPL (Europhysics Letters)*, 105(4):48004, 2014.
- [17] Yaouen Fily, Silke Henkes, and M Cristina Marchetti. Freezing and phase separation of self-propelled disks. *Soft matter*, 10(13):2132–2140, 2014.
- [18] Gabriel S Redner, Michael F Hagan, and Aparna Baskaran. Structure and dynamics of a phase-separating active colloidal fluid. *Physical review letters*, 110(5):055701, 2013.

- [19] Yaouen Fily and M Cristina Marchetti. Athermal phase separation of self-propelled particles with no alignment. *Physical review letters*, 108(23):235702, 2012.
- [20] Douglas J Durian. Foam mechanics at the bubble scale. *Physical review letters*, 75(26):4780, 1995.
- [21] Corey S O'hern, Leonardo E Silbert, Andrea J Liu, and Sidney R Nagel. Jamming at zero temperature and zero applied stress: The epitome of disorder. *Physical Review E*, 68(1):011306, 2003.
- [22] Peter Olsson and Stephen Teitel. Critical scaling of shear viscosity at the jamming transition. *Physical review letters*, 99(17):178001, 2007.
- [23] Paweł Romanczuk, Markus Bär, Werner Ebeling, Benjamin Lindner, and Lutz Schimansky-Geier. Active brownian particles. *The European Physical Journal Special Topics*, 202(1):1–162, 2012.
- [24] Ivo Buttinoni, Julian Bialké, Felix Kümmel, Hartmut Löwen, Clemens Bechinger, and Thomas Speck. Dynamical clustering and phase separation in suspensions of self-propelled colloidal particles. *Physical review letters*, 110(23):238301, 2013.
- [25] Julian Bialké, Thomas Speck, and Hartmut Löwen. Active colloidal suspensions: Clustering and phase behavior. *Journal of Non-Crystalline Solids*, 407:367–375, 2015.
- [26] Glotzer lab, University of Michigan. HOOMD-blue. URL <http://glotzerlab.engin.umich.edu/hoomd-blue/>.
- [27] Joshua A Anderson, Chris D Lorenz, and Alex Travesset. General purpose molecular dynamics simulations fully implemented on graphics processing units. *Journal of Computational Physics*, 227(10):5342–5359, 2008.
- [28] Jens Glaser, Trung Dac Nguyen, Joshua A Anderson, Pak Lui, Filippo Spiga, Jaime A Millan, David C Morse, and Sharon C Glotzer. Strong scaling of general-purpose molecular dynamics simulations on gpus. *Computer Physics Communications*, 192:97–107, 2015.
- [29] Carolyn L Phillips, Joshua A Anderson, and Sharon C Glotzer. Pseudo-random number generation for brownian dynamics and dissipative particle dynamics simulations on gpu devices. *Journal of Computational Physics*, 230(19):7191–7201, 2011.
- [30] Erik Bitzek, Pekka Koskinen, Franz Gähler, Michael Moseler, and Peter Gumbsch. Structural relaxation made simple. *Physical review letters*, 97(17):170201, 2006.
- [31] Julian Bialké, Hartmut Löwen, and Thomas Speck. Microscopic theory for the phase separation of self-propelled repulsive disks. *EPL (Europhysics Letters)*, 103(3):30008, 2013.
- [32] Kurt Binder and Walter Kob. *Glassy materials and disordered solids: An introduction to their statistical mechanics*, chapter 5.3.5. World scientific, 2011.
- [33] L Berthier. Dynamic heterogeneity in amorphous materials. *Physics*, 4:42, 2011.
- [34] Eric R Weeks, John C Crocker, and David A Weitz. Short-and long-range correlated motion observed in colloidal glasses and liquids. *Journal of Physics: Condensed Matter*, 19(20):205131, 2007.
- [35] Kurt Binder and Walter Kob. *Glassy materials and disordered solids: An introduction to their statistical mechanics*, chapter 2.1. World scientific, 2011.
- [36] Burkhard Doliwa and Andreas Heuer. Cooperativity and spatial correlations near the glass transition: Computer simulation results for hard spheres and disks. *Physical Review E*, 61(6):6898, 2000.
- [37] Andrea Cavagna. Supercooled liquids for pedestrians. *Physics Reports*, 476(4-6):51–124, 2009.
- [38] Rachel E Courtland and Eric R Weeks. Direct visualization of ageing in colloidal glasses. *Journal of Physics: Condensed Matter*, 15(1):S359, 2002.
- [39] Vishwas V Vasisht, Sudeep K Dutta, Emanuela Del Gado, and Daniel L Blair. Rate dependence of elementary rearrangements and spatiotemporal correlations in the 3d flow of soft solids. *Physical review letters*, 120(1):018001, 2018.
- [40] Michael L Falk and James S Langer. Dynamics of viscoplastic deformation in amorphous solids. *Physical Review E*, 57(6):7192, 1998.

- [41] Alexandre Nicolas, Joerg Rottler, and Jean-Louis Barrat. Spatiotemporal correlations between plastic events in the shear flow of athermal amorphous solids. *The European Physical Journal E*, 37(6):50, 2014.
- [42] John Douglas Eshelby. The elastic field outside an ellipsoidal inclusion. *Proc. R. Soc. Lond. A*, 252(1271):561–569, 1959.
- [43] Joyjit Chattoraj and Anael Lemaitre. Elastic signature of flow events in supercooled liquids under shear. *Physical review letters*, 111(6):066001, 2013.
- [44] Bernd Illing, Sebastian Fritschi, David Hajnal, Christian Klix, Peter Keim, and Matthias Fuchs. Strain pattern in supercooled liquids. *Physical review letters*, 117(20):208002, 2016.
- [45] Muhammad Hassani, Elias M Zirdehi, Kris Kok, Peter Schall, Matthias Fuchs, and Fathollah Varnik. Long-range strain correlations in 3d quiescent glass forming liquids. *arXiv preprint arXiv:1807.00090*, 2018. URL <https://arxiv.org/abs/1807.00090>.
- [46] Jeppe C Dyre. Colloquium: The glass transition and elastic models of glass-forming liquids. *Reviews of modern physics*, 78(3):953, 2006.
- [47] Lev D Landau and EM Lifshitz. *Theory of Elasticity, vol. 7*, volume 3, chapter 1, page 109. Elsevier, New York, 1986.
- [48] I Goldhirsch and C Goldenberg. On the microscopic foundations of elasticity. *The European Physical Journal E*, 9(3):245–251, 2002.
- [49] Daan Frenkel and Berend Smit. *Understanding molecular simulation: from algorithms to applications*, volume 1, chapter F.2. Elsevier, 2001.
- [50] Pablo G Debenedetti and Frank H Stillinger. Supercooled liquids and the glass transition. *Nature*, 410(6825):259, 2001.
- [51] yketa. Shear strain correlations from displacement fourier transform, Physics StackExchange, <https://physics.stackexchange.com/questions/412823>.
- [52] Christian L Klix, Florian Ebert, Fabian Weysser, Matthias Fuchs, Georg Maret, and Peter Keim. Glass elasticity from particle trajectories. *Physical review letters*, 109(17):178301, 2012.
- [53] F Leonforte, R Boissiere, Arnaud Tanguy, JP Wittmer, and J-L Barrat. Continuum limit of amorphous elastic bodies. iii. three-dimensional systems. *Physical Review B*, 72(22):224206, 2005.
- [54] Wikipedia. Ringing artifacts — Wikipedia, the free encyclopedia. https://en.wikipedia.org/wiki/Ringing_artifacts, 2018.

Appendices

A | Calculation details

A.1 Field auto-correlation

Let $\vec{v}(\vec{r})$ be a vector – or scalar – field with $\vec{r} \in \mathbb{R}^2$, then we define its auto-correlation function as

$$C_{vv}(\Delta\vec{r}) = \frac{\int d^2\vec{r} \vec{v}(\vec{r})^* \cdot \vec{v}(\vec{r} + \Delta\vec{r})}{\int d^2\vec{r} |\vec{v}(\vec{r})|^2} \quad (\text{A.1})$$

which can be efficiently calculated with the help of Fourier transforms.

We define

$$\begin{aligned} \mathcal{F} : \cdot &\mapsto \int d^2\vec{k} e^{-i\vec{k}\cdot\vec{r}} \cdot \Leftrightarrow \mathcal{F}^{-1} : \cdot &\mapsto \int d^2\vec{k} e^{i\vec{k}\cdot\vec{r}} \\ \tilde{\vec{v}} = \mathcal{F}\{\vec{v}\} &\Leftrightarrow \vec{v} = \mathcal{F}^{-1}\{\tilde{\vec{v}}\} \end{aligned} \quad (\text{A.2})$$

then

$$\begin{aligned} \int d^2\vec{r} \vec{v}(\vec{r})^* \cdot \vec{v}(\vec{r} + \Delta\vec{r}) &= \int d^2\vec{r} \left(\int d^2\vec{k} e^{i\vec{k}\cdot\vec{r}} \tilde{\vec{v}}(\vec{k}) \right)^* \cdot \left(\int d^2\vec{k}' e^{i\vec{k}'\cdot(\vec{r} + \Delta\vec{r})} \tilde{\vec{v}}(\vec{k}') \right) \\ &= \int d^2\vec{k} \int d^2\vec{k}' e^{i\vec{k}'\cdot\Delta\vec{r}} \tilde{\vec{v}}(\vec{k})^* \cdot \tilde{\vec{v}}(\vec{k}') \int d^2\vec{r} e^{-i(\vec{k}-\vec{k}')\cdot\vec{r}} \\ &= \int d^2\vec{k} \int d^2\vec{k}' e^{i\vec{k}'\cdot\Delta\vec{r}} \tilde{\vec{v}}(\vec{k})^* \cdot \tilde{\vec{v}}(\vec{k}') \delta(\vec{k} - \vec{k}') \\ &= \int d^2\vec{k} e^{i\vec{k}\cdot\Delta\vec{r}} \tilde{\vec{v}}(\vec{k})^* \cdot \tilde{\vec{v}}(\vec{k}) \\ &= \mathcal{F}^{-1}\{\mathcal{F}\{\vec{v}\}^*(\vec{k}) \cdot \mathcal{F}\{\vec{v}\}(\vec{k})\}(\Delta\vec{r}) \end{aligned} \quad (\text{A.3})$$

thus showing that C_{vv} can be easily expressed in terms of the Fourier transform of \vec{v} field.